



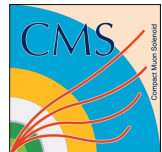
Universiteit Gent
Faculteit Wetenschappen
Vakgroep Fysica en Sterrenkunde

² No title yet

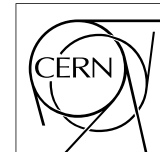
³ No sub-title neither, obviously...

⁴ Alexis Fagot

⁵



Thesis to obtain the degree of
Doctor of Philosophy in Physics
Academic years 2012-2017



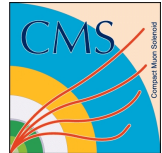


Universiteit Gent
Faculteit Wetenschappen
Vakgroep Fysica en Sterrenkunde

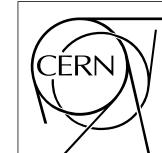
Promotoren: Dr. Michael Tytgat
Prof. Dr. Dirk Ryckbosch

Universiteit Gent
Faculteit Wetenschappen
Vakgroep Fysica en Sterrenkunde
Proeftuinstraat 86, B-9000 Gent, België
Tel.: +32 9 264.65.28
Fax.: +32 9 264.66.97

17



Thesis to obtain the degree of
Doctor of Philosophy in Physics
Academic years 2012-2017



Acknowledgements

¹⁹ Ici on remerciera tous les gens que j'ai pu croiser durant cette aventure et qui m'ont
²⁰ permis de passer un bon moment

²¹ *Gent, ici la super date de la mort qui tue de la fin d'écriture*
²² *Alexis Fagot*

Table of Contents

23

24	Acknowledgements	i
25	Nederlandse samenvatting	xvii
26	English summary	xix
27	1 Introduction	1-1
28	1.1 A story of High Energy Physics	1-1
29	1.2 Organisation of this study	1-1
30	2 Investigating the TeV scale	2-1
31	2.1 The Standard Model of Particle Physics	2-1
32	2.2 The Large Hadron Collider and the Compact Muon Solenoid	2-1
33	2.3 Muon Phase-II Upgrade	2-1
34	3 Amplification processes in gaseous detectors	3-1
35	3.1 Signal formation	3-1
36	3.2 Gas transport parameters	3-1
37	4 Resistive Plate Chambers	4-1
38	4.1 Principle	4-1
39	4.2 Rate capability of Resistive Plate Chambers	4-1
40	4.3 High time resolution	4-1
41	4.4 Resistive Plate Chambers at CMS	4-1
42	4.4.1 Overview	4-1
43	4.4.2 The present RPC system	4-2
44	4.4.3 Pulse processing of CMS RPCs	4-3
45	5 Longevity studies and Consolidation of the present CMS RPC subsystem	5-1
46	5.1 Testing detectors under extreme conditions	5-1
47	5.1.1 The Gamma Irradiation Facilities	5-3
48	5.1.1.1 GIF	5-3
49	5.1.1.2 GIF++	5-5
50	5.2 Preliminary tests at GIF	5-8
51	5.2.1 Resistive Plate Chamber test setup	5-8

53	5.2.2	Data Acquisition	5-10
54	5.2.3	Geometrical acceptance of the setup layout to cosmic muons	5-10
55	5.2.3.1	Description of the simulation layout	5-11
56	5.2.3.2	Simulation procedure	5-13
57	5.2.3.3	Results	5-14
58	5.2.4	Photon flux at GIF	5-15
59	5.2.4.1	Expectations from simulations	5-15
60	5.2.4.2	Dose measurements	5-19
61	5.2.5	Results and discussions	5-20
62	5.3	Longevity tests at GIF++	5-21
63	5.3.1	Description of the Data Acquisition	5-25
64	5.3.2	RPC current, environmental and operation parameter monitoring	5-26
65	5.3.3	Measurement procedure	5-27
66	5.3.4	Longevity studies results	5-27
68	6	Investigation on high rate RPCs	6-1
69	6.1	Rate limitations and ageing of RPCs	6-1
70	6.1.1	Low resistivity electrodes	6-1
71	6.1.2	Low noise front-end electronics	6-1
72	6.2	Construction of prototypes	6-1
73	6.3	Results and discussions	6-1
74	7	Conclusions and outlooks	7-1
75	7.1	Conclusions	7-1
76	7.2	Outlooks	7-1
77	A	A data acquisition software for CAEN VME TDCs	A-1
78	A.1	GIF++ DAQ file tree	A-1
79	A.2	Description of the readout setup	A-2
80	A.3	Data read-out	A-5
81	A.3.1	V1190A TDCs	A-5
82	A.3.2	DataReader	A-8
83	A.4	Communications	A-12
84	A.4.1	V1718 USB Bridge	A-12
85	A.4.2	Configuration file	A-13
86	A.4.3	WebDCS/DAQ intercommunication	A-15
87	A.5	DAQ algorithm overview	A-16
88	A.6	Software export	A-16
89	B	Details on the online analysis package	B-1
90	B.1	Introduction	B-1
91	C	Structure of the hybrid simulation software	C-1
92	C.1	Introduction	C-1

List of Figures

93

94	2.1	Absorbed dose in the CMS cavern after an integrated luminosity of 3000 fb. R is the transverse distance from the beamline and Z is the distance along the beamline from the Interaction Point at Z=0.	2-2
95			
96			
97	2.2	A quadrant of the muon system, showing DTs (yellow), RPCs (light blue), and CSCs (green). The locations of new forward muon detectors for Phase-II are contained within the dashed box and indicated in red for GEM stations (ME0, GE1/1, and GE2/1) and dark blue for improved RPC (iRPC) stations (RE3/1 and RE4/1).	2-3
98			
99			
100			
101			
102	2.3	RMS of the multiple scattering displacement as a function of muon p_T for the proposed forward muon stations. All of the electromag- netic processes such as bremsstrahlung and magnetic field effect are included in the simulation.	2-4
103			
104			
105			
106	4.1	Signals from the RPC strips are shaped by the FEE described on Figure 4.1a. Output LVDS signals are then read-out by a TDC module connected to a computer or converted into NIM and sent to scalers. Figure 4.1b describes how these converted signals are put in coincidence with the trigger.	4-4
107			
108			
109			
110			
111	4.2	Description of the principle of a CFD. A comparison of threshold triggering (left) and constant fraction triggering (right) is shown in Figure 4.2a. Constant fraction triggering is obtained thanks to zero-crossing technique as explained in Figure 4.2b. The signal arriving at the input of the CFD is split into three components. A first one is delayed and connected to the inverting input of a first comparator. A second component is connected to the noninverting input of this first comparator. A third component is connected to the noninverting input of another comparator along with a thresh- old value connected to the inverting input. Finally, the output of both comparators is fed through an AND gate.	4-5
112			
113			
114			
115			
116			
117			
118			
119			
120			
121			
122	5.1	(5.1a) Extrapolation from 2016 data of single hit rate per unit area in the barrel region. (5.1b) Extrapolation from 2016 data of single hit rate per unit area in the endcap region.	5-2
123			
124			

125	5.2	Background Fluka simulation compared to 2016 Data at $L = 10^{34} \text{ cm}^{-2} \cdot \text{s}^{-1}$ in the fourth endcap disk region. A mismatch in between simulation and data can be observed. [To be understood.]	5-3
128	5.3	Layout of the test beam zone called X5c GIF at CERN. Photons from the radioactive source produce a sustained high rate of random hits over the whole area. The zone is surrounded by 8 m high and 80 cm thick concrete walls. Access is possible through three entry points. Two access doors for personnel and one large gate for material. A crane allows installation of heavy equipment in the area.	5-4
135	5.4	^{137}Cs decays by β^- emission to the ground state of ^{137}Ba (BR = 5.64%) and via the 662 keV isomeric level of ^{137}Ba (BR = 94.36%) whose half-life is 2.55 min.	5-5
138	5.5	Floor plan of the GIF++ facility. When the facility downstream of the GIF++ takes electron beam, a beam pipe is installed along the beam line (z-axis). The irradiator can be displaced laterally (its center moves from $x = 0.65$ m to 2.15 m), to increase the distance to the beam pipe.	5-6
143	5.6	Simulated unattenuated current of photons in the xz plane (Figure 5.6a) and yz plane (Figure 5.6b) through the source at $x = 0.65$ m and $y = 0$ m. With angular correction filters, the current of 662 keV photons is made uniform in xy planes.	5-7
147	5.7	Description of the RPC setup. Dimensions are given in mm. A tent containing RPCs is placed at 1720 mm from the source container. The source is situated in the center of the container. RE-4-2-BARC-161 chamber is 160 mm inside the tent. This way, the distance between the source and the chambers plan is 2060 mm. Figure 5.7a provides a side view of the setup in the xz plane while Figure 5.7b shows a top view in the yz plane.	5-8
154	5.8	RE-4-2-BARC-161 chamber is inside the tent as described in Figure 5.7. In the top right, the two scintillators used as trigger can be seen. This trigger system has an inclination of 10° relative to horizontal and is placed above half-partition B2 of the RPCs. PMT electronics are shielded thanks to lead blocks placed in order to protect them without stopping photons from going through the scintillators and the chamber.	5-9

161	5.9 Hit distributions over all 3 partitions of RE-4-2-BARC-161 chamber is showed on these plots. Top, middle and bottom figures respectively correspond to partitions A, B, and C. These plots show that some events still occur in other half-partitions than B2, which corresponds to strips 49 to 64, in front of which the trigger is placed, contributing to the inefficiency of detection of cosmic muons.	5-10
171	5.10 Results are derived from data taken on half-partition B2 only. On the 18 th of June 2014, data has been taken on chamber RE-2-BARC-161 at building 904 (Prevessin Site) with cosmic muons providing us a reference efficiency plateau of $(97.54 \pm 0.15)\%$ represented by a black curve. A similar measurement has been done at GIF on the 21 st of July with the same chamber giving a plateau of $(78.52 \pm 0.94)\%$ represented by a red curve.	5-11
178	5.11 Representation of the layout used for the simulations of the test setup. The RPC is represented as a yellow trapezoid while the two scintillators as blue cuboids looking at the sky. A green plane corresponds to the muon generation plane within the simulation. Figure 5.7a shows a global view of the simulated setup. Figure 5.7b shows a zommed view that allows to see the 2 scintillators as well as the full RPC plane.	5-12
185	5.12 γ flux $F(D)$ is plot using values from table 5.1. As expected, the plot shows similar attenuation behaviours with increasing distance for each absorption factors.	5-15
188	5.13 Figure 5.13a shows the linear approximation fit done via formulae 5.7 on data from table 5.2. Figure 5.13b shows a comparison of this model with the simulated flux using a and b given in figure 5.13a in formulae 5.4 and the reference value $D_0 = 50\text{cm}$ and the associated flux for each absorption factor F_0^{ABS} from table 5.1	5-17
194	5.14 Dose measurements has been done in a plane corresponding to the tents front side. This plan is 1900 mm away from the source. As explained in the first chapter, a lens-shaped lead filter provides a uniform photon flux in the vertical plan orthogonal to the beam direction. If the second line of measured fluxes is not taken into account because of lower values due to experimental equipments in the way between the source and the tent, the uniformity of the flux is well showed by the results.	5-19
202	5.15	5-20

203	5.16 Evolution of the maximum efficiency for RE2 (5.16a) and RE4 (5.16b) chambers with increasing extrapolated γ rate per unit area at working point. Both irradiated (blue) and non irradiated (red) chambers are shown.	5-22
204		
205		
206		
207	5.17 Evolution of the working point for RE2 (5.17a) and RE4 (5.17b) with increasing extrapolated γ rate per unit area at working point. Both irradiated (blue) and non irradiated (red) chambers are shown.	5-23
208		
209		
210	5.18 Evolution of the maximum efficiency at HL-LHC conditions, i.e. a background hit rate per unit area of 300 Hz/cm ² , with increasing integrated charge for RE2 (5.18a) and RE4 (5.18b) detectors. Both irradiated (blue) and non irradiated (red) chambers are shown. The integrated charge for non irradiated detectors is recorded during test beam periods and stays small with respect to the charge accumulated in irradiated chambers.	5-23
211		
212		
213		
214		
215		
216		
217	5.19 Comparison of the efficiency sigmoid before (triangles) and after (circles) irradiation for RE2 (5.19a) and RE4 (5.19b) detectors. Both irradiated (blue) and non irradiated (red) chambers are shown.	5-24
218		
219		
220	5.20 Evolution of the Bakelite resistivity for RE2 (5.20a) and RE4 (5.20b) detectors. Both irradiated (blue) and non irradiated (red) chambers are shown.	5-24
221		
222		
223	5.21 Evolution of the noise rate per unit area for the irradiated chamber RE2-2-BARC-9 only.	5-25
224		
225	A.1 (A.1a) View of the front panel of a V1190A TDC module [10].	
226	(A.1b) View of the front panel of a V1718 Bridge module [11].	
227	(A.1c) View of the front panel of a 6U 6021 VME crate [12]. . . . A-4	
228	A.2 Module V1190A <i>Trigger Matching Mode</i> timing diagram [10]. . . A-6	
229	A.3 Structure of the ROOT output file generated by the DAQ. The 5 branches (<code>EventNumber</code> , <code>number_of_hits</code> , <code>Quality_flag</code> , <code>TDC_channel</code> and <code>TDC_TimeStamp</code>) are visible on the left panel of the ROOT browser. On the right panel is visible the histogram corresponding to the variable <code>nHits</code> . In this specific example, there were approximately 50k events recorded to measure the gamma irradiation rate on the detectors. Each event is stored as a single entry in the <code>TTree</code> . A-12	
230		
231		
232		
233		
234		
235		
236	A.4 WebDCS DAQ scan page. On this page, shifters need to choose the type of scan (Rate, Efficiency or Noise Reference scan), the gamma source configuration at the moment of data taking, the beam configuration, and the trigger mode. These information will be stored in the DAQ ROOT output. Are also given the minimal measurement time and waiting time after ramping up of the detectors is over before starting the data acquisition. Then, the list of HV points to scan and the number of triggers for each run of the scan are given in the table underneath.	A-14
237		
238		
239		
240		
241		
242		
243		
244		

List of Tables

246	5.1	Total photon flux ($E\gamma \leq 662$ keV) with statistical error predicted	
247		considering a ^{137}Cs activity of 740 GBq at different values of the	
248		distance D to the source along the x-axis of irradiation field [6]. . .	5-15
249	5.2	Correction factor c is computed thanks to formulae 5.5 taking as	
250		reference $D_0 = 50$ cm and the associated flux F_0^{ABS} for each ab-	
251		sorption factor available in table 5.1.	5-16
252	5.3	The data at D_0 in 1997 is taken from [6]. In a second step, using	
253		Equations 5.8 and 5.9, the flux at D can be estimated in 1997.	
254		Then, taking into account the attenuation of the source activity,	
255		the flux at D can be estimated at the time of the tests in GIF in	
256		2014. Finally, assuming a sensitivity of the RPC to γ $s = 2 \cdot 10^{-3}$,	
257		an estimation of the hit rate per unit area is obtained.	5-18

List of Acronyms

258

259

List of Acronyms

260

261

A

262

263

264 AFL

Almost Full Level

265

266

B

267

268

269 BARC

Bhabha Atomic Research Centre

270 BLT

Block Transfer

271 BR

Branching Ratio

272

273

C

274

275

276 CAEN

Costruzioni Apparecchiature Elettroniche Nucleari S.p.A.

277

278 CERN

European Organization for Nuclear Research

279 CFD

Constant Fraction Discriminator

280 CMS

Compact Muon Solenoid

281 CSC

Cathode Strip Chamber

282

283

D

284

285

286 DAQ

Data Acquisition

287 DCS

Detector Control Software

288 DQM

Data Quality Monitoring

289	DT	Drift Tube
290		
291		
292	F	
293		
294	FEE	Front-End Electronics
295	FEB	Front-End Board
296		
297		
298	G	
299		
300	GE/-	Find a good description
301	GE1/1	Find a good description
302	GE2/1	Find a good description
303	GEANT	GEometry ANd Tracking - a series of software toolkit platforms developed by CERN
304		
305	GEM	Gas Electron Multiplier
306	GIF	Gamma Irradiation Facility
307	GIF++	new Gamma Irradiation Facility
308		
309		
310	H	
311		
312	HL-LHC	High Luminosity LHC
313	HV	High Voltage
314		
315		
316	I	
317		
318	iRPC	improved RPC
319	IRQ	Interrupt Request
320		
321		
322	L	
323		
324	LHC	Large Hadron Collider
325	LS1	First Long Shutdown
326	LS3	Third Long Shutdown

327	LV	Low Voltage
328	LVDS	Low-Voltage Differential Signaling
329		
330		
331	M	
332		
333	MC	Monte Carlo
334	MCNP	Monte Carlo N-Particle
335	ME-/-	Find good description
336	ME0	Find good description
337		
338		
339	N	
340		
341	NIM	Nuclear Instrumentation Module logic signals
342		
343		
344	P	
345		
346	PMT	PhotoMultiplier Tube
347		
348		
349	R	
350		
351	RE-/-	Find a good description
352	RE2/2	Find a good description
353	RE3/1	Find a good description
354	RE3/2	Find a good description
355	RE4/1	Find a good description
356	RE4/2	Find a good description
357	RE4/3	Find a good description
358	RMS	Root Mean Square
359	ROOT	a framework for data processing born at CERN
360	RPC	Resistive Plate Chamber
361		
362		
363	S	
364		
365	SPS	Super Proton Synchrotron

366		
367	T	
368		
369		
370	TDC	Time-to-Digital Converter
371		
372		
373	W	
374		
375	webDCS	Web Detector Control System

377

Nederlandse samenvatting –Summary in Dutch–

378

379 Le resume en Neerlandais (j'aurais peut-etre de apprendre la langue juste pour
380 ca...).

English summary

³⁸² Le meme résume mais en Anglais (on commencera par la hein!).

1

Introduction

383

384

385 1.1 A story of High Energy Physics

386 1.2 Organisation of this study

2

387

388

Investigating the TeV scale

389 2.1 The Standard Model of Particle Physics

390 2.2 The Large Hadron Collider and the Compact 391 Muon Solenoid

392 2.3 Muon Phase-II Upgrade

393 After the more than two years lasting First Long Shutdown (LS1), the Large
394 Hadron Collider (LHC) delivered its very first Run-II proton-proton collisions
395 early 2015. LS1 gave the opportunity to the LHC and to its experiments to
396 undergo upgrades. The accelerator is now providing collisions at center-of-mass
397 energy of 13 TeV and bunch crossing rate of 40 MHz, with a peak luminosity ex-
398 ceeding its design value. During the first and upcoming second LHC Long Shut-
399 down, the Compact Muon Solenoid (CMS) detector is also undergoing a number
400 of upgrades to maintain a high system performance [1].

401 From the LHC Phase-II or High Luminosity LHC (HL-LHC) period onwards,
402 i.e. past the Third Long Shutdown (LS3), the performance degradation due to
403 integrated radiation as well as the average number of inelastic collisions per bunch
404 crossing, or pileup, will rise substantially and become a major challenge for the
405 LHC experiments, like CMS that are forced to address an upgrade program for
406 Phase-II [2]. Simulations of the expected distribution of absorbed dose in the CMS
407 detector under HL-LHC conditions, show in figure 5.14 that detectors placed close

- ⁴⁰⁸ to the beamline will have to withstand high irradiation, the radiation dose being of
⁴⁰⁹ the order of a few tens of Gy.

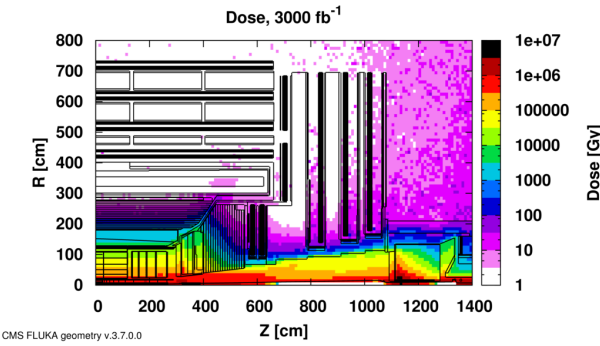


Figure 2.1: Absorbed dose in the CMS cavern after an integrated luminosity of 3000 fb. R is the transverse distance from the beamline and Z is the distance along the beamline from the Interaction Point at Z=0.

⁴¹⁰ The measurement of small production cross-section and/or decay branching
⁴¹¹ ratio processes, such as the Higgs boson coupling to charge leptons or the $B_s \rightarrow$
⁴¹² $\mu^+ \mu^-$ decay, is of major interest and specific upgrades in the forward regions of
⁴¹³ the detector will be required to maximize the physics acceptance on the largest
⁴¹⁴ possible solid angle. To ensure proper trigger performance within the present cov-
⁴¹⁵ erage, the muon system will be completed with new chambers. In figure 2.2 one
⁴¹⁶ can see that the existing Cathode Strip Chambers (CSCs) will be completed by Gas
⁴¹⁷ Electron Multipliers (GEMs) and Resistive Plate Chambers (RPCs) in the pseudo-
⁴¹⁸ rapidity region $1.6 < |\eta| < 2.4$ to complete its redundancy as originally scheduled
⁴¹⁹ in the CMS Technical Proposal [3].

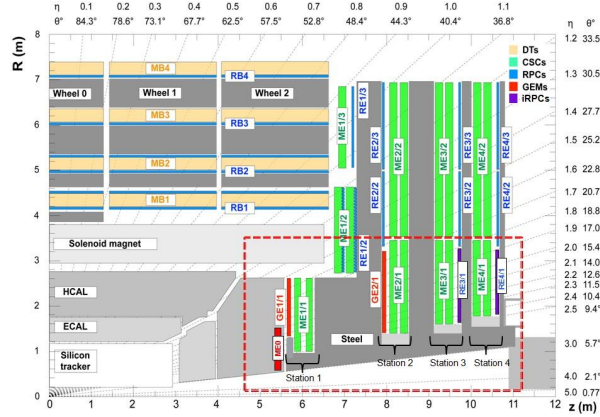


Figure 2.2: A quadrant of the muon system, showing DTs (yellow), RPCs (light blue), and CSCs (green). The locations of new forward muon detectors for Phase-II are contained within the dashed box and indicated in red for GEM stations (ME0, GE1/1, and GE2/1) and dark blue for improved RPC (iRPC) stations (RE3/1 and RE4/1).

420 RPCs are used by the CMS first level trigger for their good timing performances.
 421 Indeed, a very good bunch crossing identification can be obtained with the
 422 present CMS RPC system, given their fast response of the order of 1 ns. In order
 423 to contribute to the precision of muon momentum measurements, muon chambers
 424 should have a spatial resolution less or comparable to the contribution of multiple
 425 scattering [1]. Most of the plausible physics is covered only considering muons
 426 with $p_T < 100$ GeV thus, in order to match CMS requirements, a spatial resolu-
 427 tion of $\mathcal{O}(\text{few mm})$ the proposed new RPC stations, as shown by the simulation in
 428 figure 2.3. According to preliminary designs, RE3/1 and RE4/1 readout pitch will
 429 be comprised between 3 and 6 mm and 5 η -partitions could be considered.

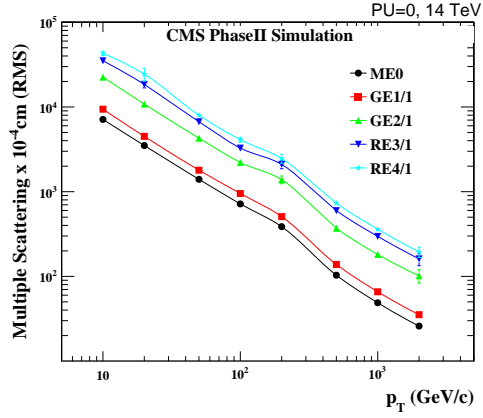


Figure 2.3: RMS of the multiple scattering displacement as a function of muon p_T for the proposed forward muon stations. All of the electromagnetic processes such as bremsstrahlung and magnetic field effect are included in the simulation.

3

430

431

432

Amplification processes in gaseous detectors

433 **3.1 Signal formation**

434 **3.2 Gas transport parameters**

4

435

436

Resistive Plate Chambers

437 **4.1 Principle**

438 **4.2 Rate capability of Resistive Plate Chambers**

439 **4.3 High time resolution**

440 **4.4 Resistive Plate Chambers at CMS**

441 **4.4.1 Overview**

442 The Resistive Plate Chambers (RPC) system, located in both barrel and endcap
443 regions, provides a fast, independent muon trigger with a looser p_T threshold over
444 a large portion of the pseudorapidity range ($|\eta| < 1.6$) [\[add reconstruction\]](#).

445

446 During High-Luminosity LHC (HL-LHC) operations the expected conditions
447 in terms of background and pile-up will make the identification and correct P_T as-
448 signment a challenge for the Muon system. The goal of RPC upgrade is to provide
449 additional hits to the Muon system with precise timing. All these informations will
450 be elaborated by the trigger system in a global way enhancing the performance of
451 the trigger in terms of efficiency and rate control. The RPC Upgrade is based
452 on two projects: an improved Link Board System and the extension of the RPC
453 coverage up to $|\eta| = 2.4$. [\[FIXME 2.4 or 2.5?\]](#)

454 The Link Board system, that will be described in section xxx, is responsible to
455 process, synchronize and zero-suppress the signals coming from the RPC front end
456 boards. The Link Board components have been produced between 2006 and 2007
457 and will be subjected to aging and failure in the long term. The upgraded Link
458 Board system will overcome the aging problems described in section xxx and will
459 allow for a more precise timing information to the RPC hits from 25 to 1 ns [ref
460 section xxx].

461 The extension of the RPC system up to $|\eta| = 2.1$ was already planned in the
462 CMS TDR [ref cmstdr] and staged because of budget limitations and expected
463 background rates higher than the rate capability of the present CMS RPCs in that
464 region. An extensive R&D program has been done in order to develop an improved
465 RPC that fulfills the CMS requirements. Two new RPC layers in the innermost ring
466 of stations 3 and 4 will be added with benefits to the neutron-induced background
467 reduction and efficiency improvement for both trigger and offline reconstruction.

468 4.4.2 The present RPC system

469 The RPC system is organized in 4 stations called RB1 to RB4 in the barrel region,
470 and RE1 to RE4 in the endcap region. The innermost barrel stations, RB1 and
471 RB2, are instrumented with 2 layers of RPCs facing the innermost (RB1in and
472 RB2in) and outermost (RB1out and RB2out) sides of the DT chambers. Every
473 chamber is then divided from the read-out point of view into 2 or 3 η partitions
474 called “rolls”. The RPC system consist of 480 barrel chambers and 576 endcap
475 chambers. Details on the geometry are discussed in the paper [ref to geo paper].

476 The CMS RPC chamber is a double-gap, operated in avalanche mode to ensure
477 reliable operation at high rates. Each RPC gap consists of two 2-mm-thick resistive
478 High-Pressure Laminate (HPL) plates separated by a 2-mm-thick gas gap. The
479 outer surface of the HPL plates is coated with a thin conductive graphite layer, and
480 a voltage is applied. The RPCs are operated with a 3-component, non-flammable
481 gas mixture consisting of 95.2% freon ($C_2H_2F_4$, known as R134a), 4.5% isobutane
482 ($i-C_4H_{10}$), and 0.3% sulphur hexafluoride (SF_6) with a relative humidity of 40% -
483 50%. Readout strips are aligned in η between the 2 gas gaps. [\[Add a sentence on
484 FEBs.\]](#)

485 The discriminated signals coming from the Front End boards feed via twisted
486 cables (10 to 20 m long) the Link Board System located in UXC on the balconies
487 around the detector. The Link System consist of the 1376 Link Boards (LBs)
488 and the 216 Control Boards (CBs), placed in 108 Link Boxes. The Link Box
489 is a custom crate (6U high) with 20 slots (for two CBs and eighteen LBs). The
490 Link Box contains custom backplane to which the cables from the chambers are
491 connected, as well as the cables providing the LBs and CBs power supply and the
492 cables for the RPC FEBs control with use of the I2C protocol (trough the CB). The

493 backplane itself contains only connectors (and no any other electronic devices).

494 The Link Board has 96 input channels (one channel corresponds to one RPC
495 strip). The input signals are the ~ 100 ns binary pulses which are synchronous to
496 the RPC hits, but not to the LHC clock (which drives the entire CMS electronics).
497 Thus the first step of the FEB signals processing is synchronization, i.e. assign-
498 ment of the signals to the BXes (25 ns periods). Then the data are compressed with
499 a simple zero-suppressing algorithm (the input channels are grouped into 8 bit par-
500 titions, only the partitions with at least one nonzero bit are selected for each BX).
501 Next, the non-empty partitions are time-multiplexed i.e. if there are more than one
502 such partition in a given BX, they are sent one-by-one in consecutive BXes. The
503 data from 3 neighbouring LBs are concentrated by the middle LB which contains
504 the optical transmitter for sending them to the USC over a fiber at 1.6 Gbps.

505 The Control Boards provide the communication of the control software with
506 the LBs via the FEC/CCU system. The CBs are connected into token rings, each
507 ring consists of 12 CBs of one detector tower and a FEC mezzanine board placed
508 on the CCS board located in the VME crate in the USC. In total, there are 18 rings
509 in the entire Link System. The CBs also perform automatic reloading of the LB's
510 firmware which is needed in order to avoid accumulation of the radiation induced
511 SEUs in the LBs firmware.

512 Both LBs and CB are based on the Xilinx Spartan III FPGAs, the CB addition-
513 ally contains radiation-tolerant (FLASH based) FPGA Actel ProAsicPlus.

514 The High Voltage power system is located in USC, not exposed to radiation and
515 easily accessible for any reparation. A single HV channel powers 2 RPC chambers
516 both in the barrel and endcap regions. The Low Voltage boards are located in UXC
517 on the balconies and provide the voltage to the front end electronics.

518 **4.4.3 Pulse processing of CMS RPCs**

519 Signals induced by cosmic particle in the RPC strips are shaped by standard CMS
520 RPC Front-End Electronics (FEE) following the scheme of Figure 4.1. On a first
521 stage, analogic signals are amplified and then sent to the Constant Fraction Dis-
522 criminator (CFD) described in Figure 4.2. At the end of the chain, 100 ns long
523 pulses are sent in the LVDS output. These output signal are sent on one side to a
524 V1190A Time-to-Digital Converter (TDC) module from CAEN and on the other
525 to an OR module to count the number of detected signals. Trigger and hit coïnci-
526 dences are monitored using scalers. The TDC is used to store the data into ROOT
527 files. These files are thus analysed to understand the detectors performance.

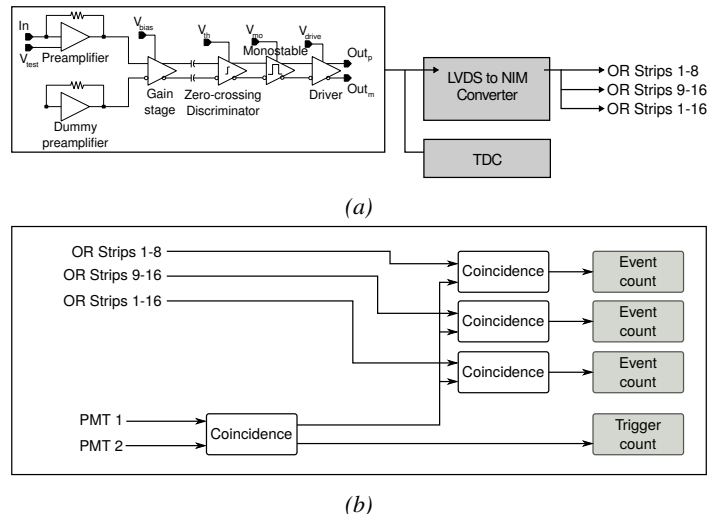


Figure 4.1: Signals from the RPC strips are shaped by the FEE described on Figure 4.1a. Output LVDS signals are then read-out by a TDC module connected to a computer or converted into NIM and sent to scalers. Figure 4.1b describes how these converted signals are put in coincidence with the trigger.

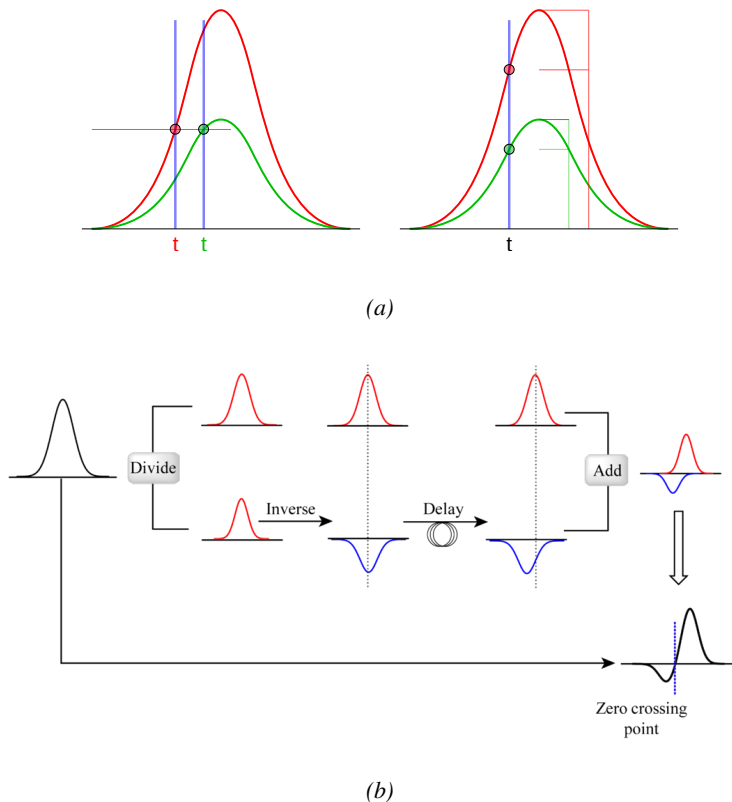


Figure 4.2: Description of the principle of a CFD. A comparison of threshold triggering (left) and constant fraction triggering (right) is shown in Figure 4.2a. Constant fraction triggering is obtained thanks to zero-crossing technique as explained in Figure 4.2b. The signal arriving at the input of the CFD is split into three components. A first one is delayed and connected to the inverting input of a first comparator. A second component is connected to the noninverting input of this first comparator. A third component is connected to the noninverting input of another comparator along with a threshold value connected to the inverting input. Finally, the output of both comparators is fed through an AND gate.

5

528

529 Longevity studies and Consolidation of 530 the present CMS RPC subsystem

531 **5.1 Testing detectors under extreme conditions**

532 The upgrade from LHC to HL-LHC will increase the peak luminosity from 10^{34}
533 $\text{cm}^{-2} \text{s}^{-1}$ to reach $5 \times 10^{34} \text{ cm}^{-2} \text{s}^{-1}$, increasing in the same way the total ex-
534 pected background to which the RPC system will be subjected to. Composed of
535 low energy gammas and neutrons from p - p collisions, low momentum primary
536 and secondary muons, puch-through hadrons from calorimeters, and particles pro-
537 duced in the interaction of the beams with collimators, the background will mostly
538 affect the regions of CMS that are the closest to the beam line, i.e. the RPC detec-
539 tors located in the endcaps. [\[To update.\]](#)

540

541 The 2016 data allowed to study the values of the background rate in all RPC
542 system. In Figure 5.1, the distribution of the chamber background hit rate per unit
543 area is shown at a luminosity of $5 \times 10^{34} \text{ cm}^{-2} \cdot \text{s}^{-1}$ linearly extrapolating from
544 data collected in 2016 [\[ref mentioning the linear dependency of rate vs lumi\]](#). The
545 maximum rate per unit area at HL-LHC conditions is expected to be of the or-
546 der of 600 Hz/cm^2 (including a safety factor 3). Nevertheless, Fluka simulations
547 have conducted in order to understand the background at HL-LHC conditions. The
548 comparison to the data has shown, in Figure 5.2, a discrepancy of a factor 2 even
549 though the order of magnitude is consistent. [\[Understand mismatch.\]](#)

550

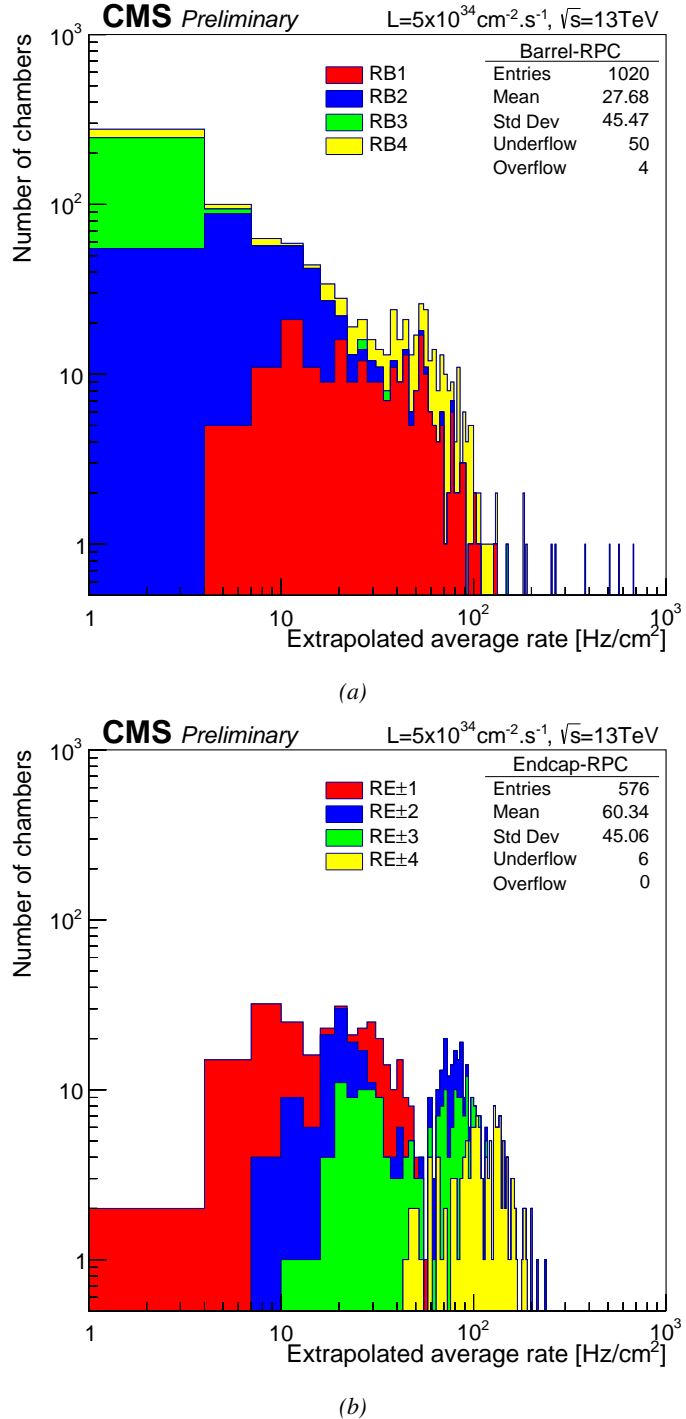


Figure 5.1: (5.1a) Extrapolation from 2016 data of single hit rate per unit area in the barrel region. (5.1b) Extrapolation from 2016 data of single hit rate per unit area in the endcap region.

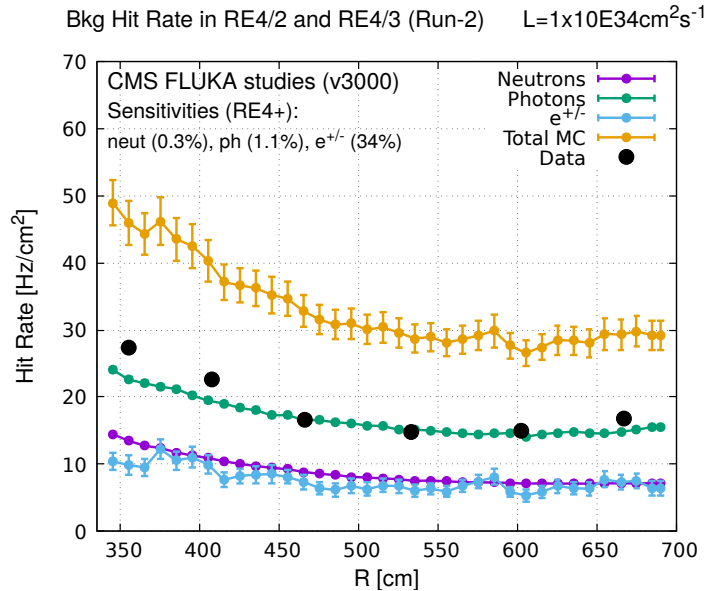


Figure 5.2: Background Fluka simulation compared to 2016 Data at $L = 10^{34} \text{ cm}^{-2} \cdot \text{s}^{-1}$ in the fourth endcap disk region. A mismatch in between simulation and data can be observed. [To be understood.]

551 In the past, extensive long-term tests were carried out at several gamma and
 552 neutron facilities certifying the detector performance. Both full size and small
 553 prototype RPCs have been irradiated with photons up to an integrated charge of
 554 $\sim 0.05 \text{ C}/\text{cm}^2$ and $\sim 0.4 \text{ C}/\text{cm}^2$, respectively [4, 5]. During Run-I, the RPC sys-
 555 tem provided stable operation and excellent performance and did not show any
 556 aging effects for integrated charge of the order of $0.01 \text{ C}/\text{cm}^2$. Projections on cur-
 557 rents from 2016 Data, has allowed to determine that the total integrated charge, by
 558 the end of HL-LHC, would be of the order of $1 \text{ C}/\text{cm}^2$ (including a safety factor
 559 3). [Corresponding figure needed.]

560

561 5.1.1 The Gamma Irradiation Facilities

562 5.1.1.1 GIF

563 Located in the SPS West Area at the downstream end of the X5 test beam, the
 564 Gamma Irradiation Facility (GIF) was a test area in which particle detectors were
 565 exposed to a particle beam in presence of an adjustable gamma background [6].
 566 Its goal was to reproduce background conditions these detectors would suffer in
 567 their operating environment at LHC. GIF layout is shown in Figure 5.3. Gamma

568 photons are produced by a strong ^{137}Cs source installed in the upstream part of the
 569 zone inside a lead container. The source container includes a collimator, designed
 570 to irradiate a $6 \times 6 \text{ m}^2$ area at 5 m maximum to the source. A thin lens-shaped lead
 571 filter helps providing with a uniform outgoing flux in a vertical plane, orthogonal
 572 to the beam direction. The principal collimator hole provides a pyramidal aperture
 573 of $74^\circ \times 74^\circ$ solid angle and provides a photon flux in a pyramidal volume along
 574 the beam axis. The photon rate is controled by further lead filters allowing the
 575 maximum rate to be limited and to vary within a range of four orders of magni-
 576 tude. Particle detectors under test are then placed within the pyramidal volume
 577 in front of the source, perpendicularly to the beam line in order to profit from the
 578 homogeneous photon flux. Adjusting the background flux of photons can then be
 579 done by using the filters and choosing the position of the detectors with respect to
 580 the source.

581

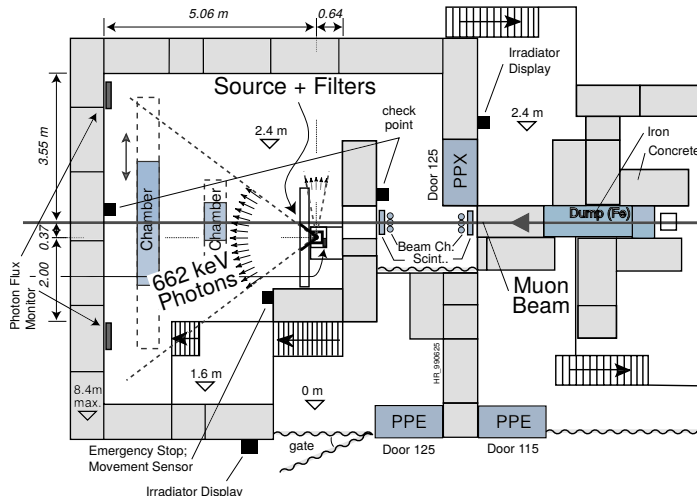


Figure 5.3: Layout of the test beam zone called X5c GIF at CERN. Photons from the radioactive source produce a sustained high rate of random hits over the whole area. The zone is surrounded by 8 m high and 80 cm thick concrete walls. Access is possible through three entry points. Two access doors for personnel and one large gate for material. A crane allows installation of heavy equipment in the area.

582 As described on Figure 5.4, the ^{137}Cs source emits a 662 keV photon in 85%
 583 of the decays. An activity of 740 GBq was measured on the 5th March 1997. To
 584 estimate the strength of the flux in 2014, it is necessary to consider the nuclear
 585 decay through time assiciated to the Cesium source whose half-life is well known
 586 ($t_{1/2} = (30.05 \pm 0.08) \text{ y}$). The GIF tests where done in between the 20th and the
 587 31st of August 2014, i.e. at a time $t = (17.47 \pm 0.02) \text{ y}$ resulting in an attenuation

588 of the activity from 740 GBq in 1997 to 494 GBq in 2014.

589

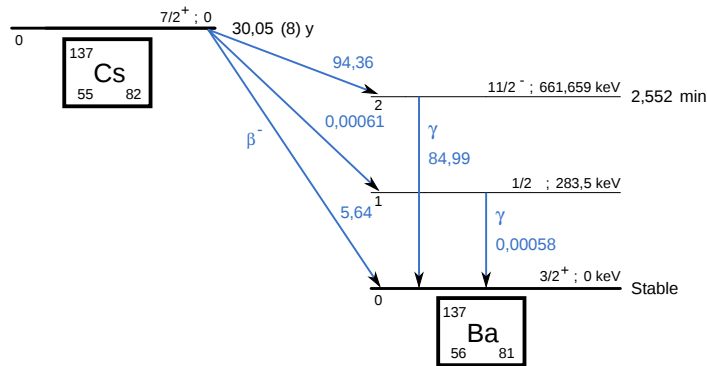


Figure 5.4: ^{137}Cs decays by β^- emission to the ground state of ^{137}Ba ($BR = 5.64\%$) and via the 662 keV isomeric level of ^{137}Ba ($BR = 94.36\%$) whose half-life is 2.55 min.

590 5.1.1.2 GIF++

591 The new Gamma Irradiation Facility (GIF++), located in the SPS North Area at
 592 the downstream end of the H4 test beam, has replaced its predecessor during LS1
 593 and has been operational since spring 2015 [7]. Like GIF, GIF++ features a ^{137}Cs
 594 source of 662 keV gamma photons, their fluence being controlled with a set of
 595 filters of various attenuation factors. The source provides two separated large irra-
 596 diation areas for testing several full-size muon detectors with continuous homo-
 597 geneous irradiation, as presented in Figure 5.5.

598

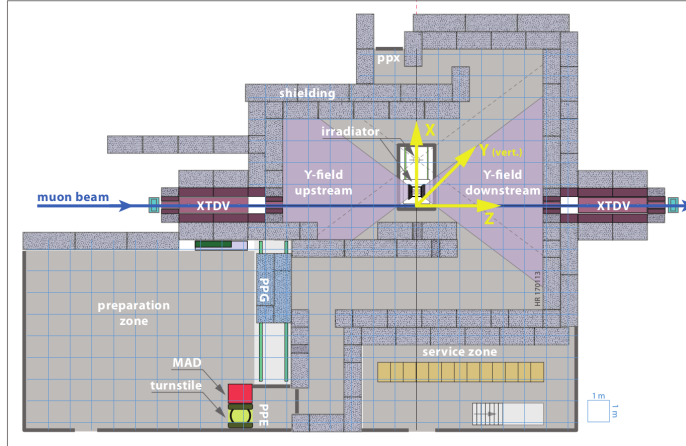


Figure 5.5: Floor plan of the GIF++ facility. When the facility downstream of the GIF++ takes electron beam, a beam pipe is installed along the beam line (z -axis). The irradiator can be displaced laterally (its center moves from $x = 0.65$ m to 2.15 m), to increase the distance to the beam pipe.

599 The source activity was measured to be about 13.5 TBq in March 2016. The
 600 photon flux being far greater than HL-LHC expectations, GIF++ provides an ex-
 601 cellent facility for accelerated aging tests of muon detectors.
 602

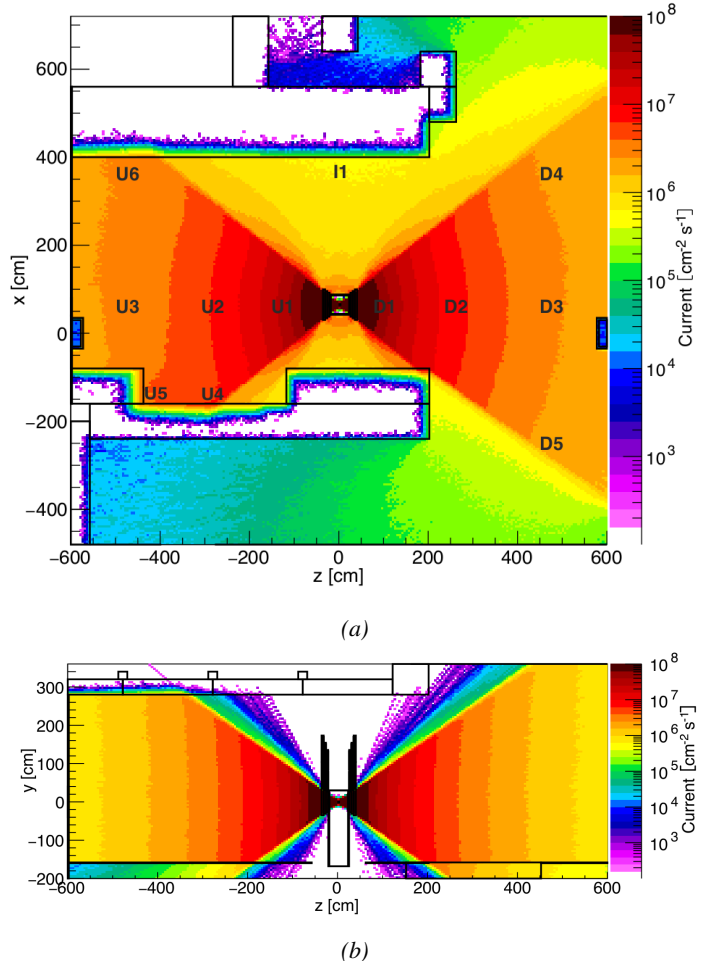


Figure 5.6: Simulated unattenuated current of photons in the xz plane (Figure 5.6a) and yz plane (Figure 5.6b) through the source at $x = 0.65$ m and $y = 0$ m. With angular correction filters, the current of 662 keV photons is made uniform in xy planes.

603 The source is situated in the muon beam line with the muon beam being avail-
 604 able a few times a year. The H4 beam, composed of muons with a momentum of
 605 about 150 GeV/c, passes through the GIF++ zone and is used to study the per-
 606 formance of the detectors. Its flux is of 104 particles/s/cm² focused in an area
 607 similar to 10×10 cm². Therefore, with properly adjusted filters, one can imitate
 608 the HL-LHC background and study the performance of muon detectors with their
 609 trigger/readout electronics in HL-LHC environment.
 610

611 5.2 Preliminary tests at GIF

612 5.2.1 Resistive Plate Chamber test setup

613 During summer 2014, preliminary tests have been conducted in the GIF area on
 614 a newly produced RE4/2 chamber labelled RE-4-2-BARC-161. This chamber has
 615 been placed into a trolley covered with a tent. The position of the RPC inside the
 616 tent and of the tent related to the source is described in Figure 5.7. To test this
 617 CMS RPC, three different absorber settings were used. First of all, measurements
 618 were done with fully opened source. Then, to complete this preliminary study,
 619 the gamma flux has been attenuated from a factor 2 and a factor 5. The expected
 620 gamma flux at the level of our detector will be discussed in subsection 5.2.4.

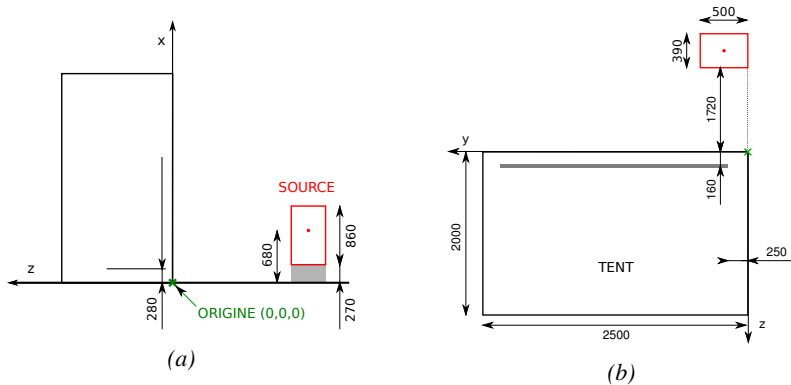


Figure 5.7: Description of the RPC setup. Dimensions are given in mm. A tent containing RPCs is placed at 1720 mm from the source container. The source is situated in the center of the container. RE-4-2-BARC-161 chamber is 160 mm inside the tent. This way, the distance between the source and the chambers plan is 2060 mm. Figure 5.7a provides a side view of the setup in the xz plane while Figure 5.7b shows a top view in the yz plane.



Figure 5.8: RE-4-2-BARC-161 chamber is inside the tent as described in Figure 5.7. In the top right, the two scintillators used as trigger can be seen. This trigger system has an inclination of 10° relative to horizontal and is placed above half-partition B2 of the RPCs. PMT electronics are shielded thanks to lead blocks placed in order to protect them without stopping photons from going through the scintillators and the chamber.

621 At the time of the tests, the beam not being operational anymore, a trigger
622 composed of 2 plastic scintillators has been placed in front of the setup with an
623 inclination of 10° deg with respect to the detector plane in order to look at cosmic
624 muons. Using this particular trigger layout, shown on Figure 5.8, leads to a cosmic
625 muon hit distribution into the chamber similar to the one in Figure 5.9. Measured
626 without gamma irradiation, two peaks can be seen on the profil of partition B, cen-
627 tered on strips 52 and 59. Section 5.2.3 will help us understand that these two peaks
628 are due respectively to forward and backward coming cosmic particles where for-
629 ward coming particles are first detected by the scintillators and then the RPC while
630 the backward coming muons are first detected in the RPC.

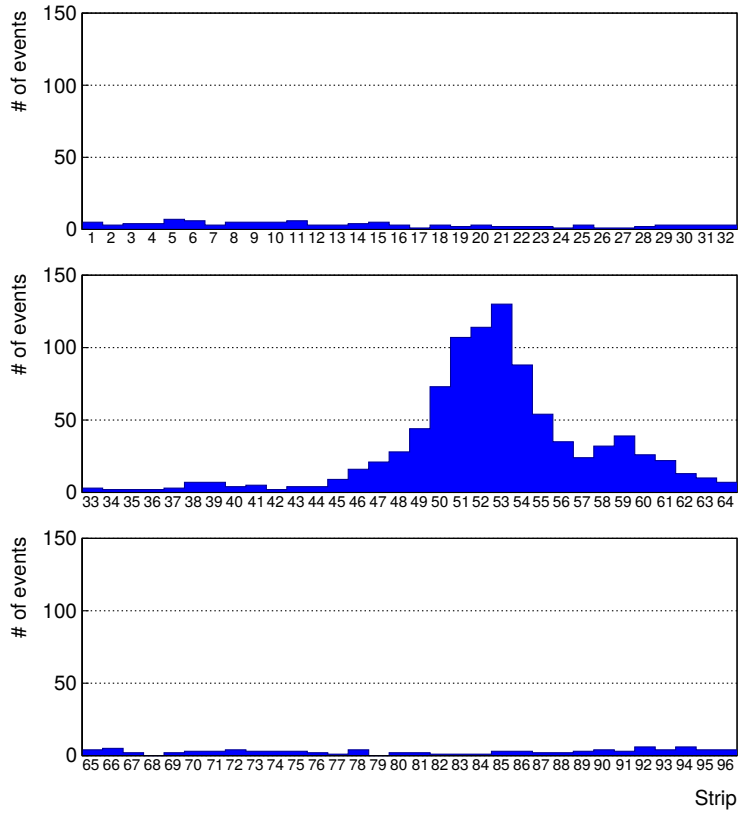


Figure 5.9: Hit distributions over all 3 partitions of RE-4-2-BARC-161 chamber is showed on these plots. Top, middle and bottom figures respectively correspond to partitions A, B, and C. These plots show that some events still occur in other half-partitions than B2, which corresponds to strips 49 to 64, in front of which the trigger is placed, contributing to the inefficiency of detection of cosmic muons. In the case of partitions A and C, the very low amount of data can be interpreted as noise. On the other hand, it is clear that a little portion of muons reach the half-partition B1, corresponding to strips 33 to 48.

5.2.2 Data Acquisition

5.2.3 Geometrical acceptance of the setup layout to cosmic muons

In order to profit from a constant gamma irradiation, the detectors inside of the GIF bunker need to be placed in a plane orthogonal to the beam line. The muon beam that used to be available was meant to test the performance of detectors under test. This beam not being active anymore, another solution to test detector performance had to be used. Thus, it has been decided to use cosmic muons detected through

638 a telescope composed of two scintillators. Lead blocks were used as shielding to
 639 protect the photomultipliers from gammas as can be seen from Figure 5.8.

640 An inclination has been given to the cosmic telescope to maximize the muon
 641 flux. A good compromise had to be found between good enough muon flux and
 642 narrow enough hit distribution to be sure to contain all the events into only one half
 643 partitions as required from the limited available readout hardware. Nevertheless,
 644 a consequence of the misplaced trigger, that can be seen as a loss of events in
 645 half-partition B1 in Figure 5.9, is an inefficiency. Nevertheless, the inefficiency
 646 of approximately 20 % highlighted in Figure 5.10 by comparing the performance
 647 of chamber BARC-161 in 904 and at GIF without irradiation seems too important
 648 to be explained only by the geometrical acceptance of the setup itself. Simulations
 649 have been conducted to show how the setup brings inefficiency.

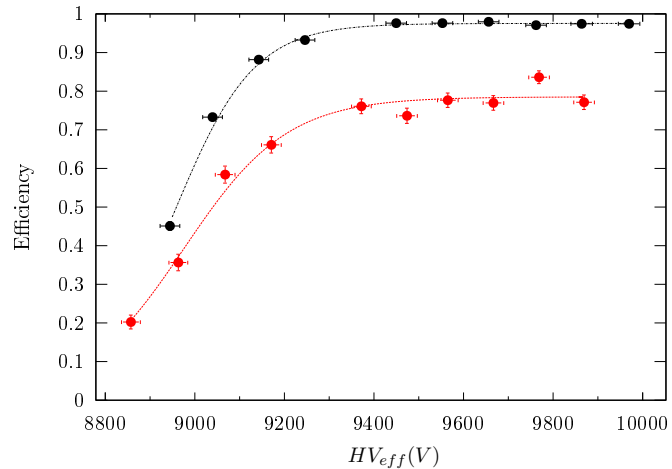


Figure 5.10: Results are derived from data taken on half-partition B2 only. On the 18th of June 2014, data has been taken on chamber RE-2-BARC-161 at building 904 (Prevessin Site) with cosmic muons providing us a reference efficiency plateau of $(97.54 \pm 0.15)\%$ represented by a black curve. A similar measurement has been done at GIF on the 21st of July with the same chamber giving a plateau of $(78.52 \pm 0.94)\%$ represented by a red curve.

650 5.2.3.1 Description of the simulation layout

651 The layout of GIF setup has been reproduced and incorporated into a Monte Carlo
 652 (MC) simulation to study the influence of the disposition of the telescope on the
 653 final distribution measured by the RPC. A 3D view of the simulated layout is given
 654 into Figure 5.11. Muons are generated randomly in a horizontal plane located at a
 655 height corresponding to the lowest point of the PMTs. This way, the needed size
 656 of the plane in order to simulate events happening at very big azimuthal angles (i.e.

657 $\theta \approx \pi$) can be kept relatively small. The muon flux is designed to follow the usual
 658 $\cos^2\theta$ distribution for cosmic particle. The goal of the simulation is to look at
 659 muons that pass through the muon telescope composed of the two scintillators and
 660 define their distribution onto the RPC plane. During the reconstruction, the RPC
 661 plane is then divided into its strips and each muon track is assigned to a strip.

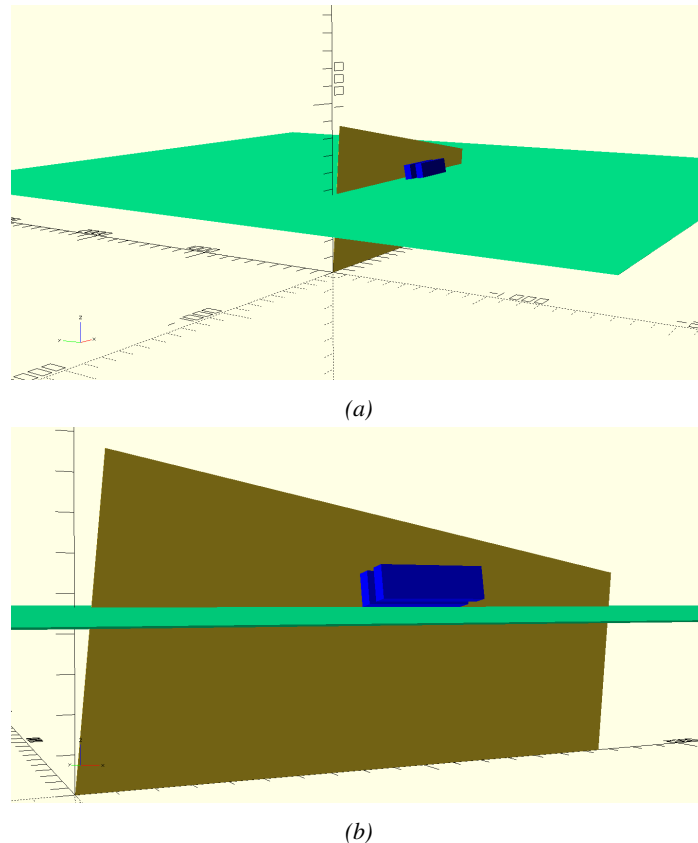


Figure 5.11: Representation of the layout used for the simulations of the test setup. The RPC is represented as a yellow trapezoid while the two scintillators as blue cuboids looking at the sky. A green plane corresponds to the muon generation plane within the simulation. Figure 5.7a shows a global view of the simulated setup. Figure 5.7b shows a zoomed view that allows to see the 2 scintillators as well as the full RPC plane.

662 In order to further refine the quality of the simulation and understand deeper
 663 the results the dependance of the distribution has been studied for a range of tele-
 664 scope inclinations. Moreover, the threshold applied on the PMT signals has been
 665 included into the simulation in the form of a cut. In the approximation of uni-
 666 form scintillators, it has been considered that the threshold can be understood as

667 the minimum distance particles need to travel through the scintillating material to
668 give a strong enough signal. Particles that travel a distance smaller than the set
669 "threshold" are thus not detected by the telescope and cannot trigger the data tak-
670 ing. Finally, the FEE threshold also has been considered in a similar way. The
671 mean momentum of horizontal cosmic rays is higher than those of vertical ones
672 but the stopping power of matter for momenta ranging from 1 GeV to 1 TeV stays
673 comparable. It is then possible to assume that the mean number of primary e^-/ion
674 pairs per unit length will stay similar and thus, depending on the applied discrimi-
675 nator threshold, muons with the shortest path through the gas volume will deposit
676 less charge and induce a smaller signal on the pick-up strips that could eventu-
677 ally not be detected. These two thresholds also restrain the overall geometrical
678 acceptance of the system.

679 **5.2.3.2 Simulation procedure**

680 The simulation software has been designed using C++ and the output data is saved
681 into ROOT histograms. Simulations start for a threshold T_{scint} varying in a range
682 from 0 to 45 mm in steps of 5 mm, where $T_{scint} = 0$ mm corresponds to the case
683 where there isn't any threshold apply on the input signal while $T_{scint} = 45$ mm,
684 which is the scintillator thickness, is the case where muons cannot arrive orthogo-
685 nally onto the scintillator surface. For a given T_{scint} , a set of RPC thresholds are
686 considered. The RPC threshold, T_{RPC} varies from 2 mm, the thickness of the gas
687 volume, to 3 mm in steps of 0.25 mm. For each $(T_{scint}; T_{RPC})$ pair, $N_\mu = 10^8$
688 muons are randomly generated inside the muon plane described in the previous
689 paragraph with an azimuthal angle θ chosen to follow a $\cos^2\theta$ distribution.

690 Planes are associated to each surface of the scintillators. Knowing muon posi-
691 tion into the muon plane and its direction allows us, by assuming that muons travel
692 in a straight line, to compute the intersection of the muon track with these planes.
693 Applying conditions to the limits of the surfaces of the scintillator faces then gives
694 us an answer to whether or not the muon passed through the scintillators. In the
695 case the muon has indeed passed through the telescope, the path through each scin-
696 tillator is computed and muons whose path was shorter than T_{scint} are rejected and
697 are thus considered as having not interacted with the setup.

698 On the contrary, if the muon is labeled as good, its position within the RPC
699 plane is computed and the corresponding strip, determined by geometrical tests
700 in the case the distance through the gas volume was enough not to be rejected
701 because of T_{RPC} , gets a hit and several histograms are filled in order to keep
702 track of the generation point on the muon plane, the intersection points of the
703 reconstructed muons within the telescope, or on the RPC plane, the path traveled
704 through each individual scintillator or the gas volume, as well as other histograms.
705 Moreover, muons fill different histograms whether they are forward or backward
706 coming muons. They are discriminated according to their direction components.

707 When a muon is generated, an (x, y, z) position is assigned into the muon plane as
 708 well as a $(\theta; \phi)$ pair that gives us the direction it's coming from. This way, muons
 709 satisfying the condition $0 \leq \phi < \pi$ are designated as backward coming muons
 710 while muons satisfying $\pi \leq \phi < 2\pi$ as forward coming muons.

711 This simulation is then repeated for different telescope inclinations ranging in
 712 between 4 and 20° and varying in steps of 2° . Due to this inclination and to the
 713 vertical position of the detector under test, the muon distribution reconstructed in
 714 the detector plane is asymmetrical. The choice has been made to chose a skew
 715 distribution formula to fit the data built as the multiplication of gaussian and sig-
 716 moidal curves together. A typical gaussian formula is given as 5.1 and has three
 717 free parameters as A_g , its amplitude, \bar{x} , its mean value and σ , its root mean square.
 718 Sigmoidal curves as given by formula 5.2 are functions converging to 0 and A_s as
 719 x diverges. The inflexion point is given as x_i and λ is proportional to the slope at
 720 $x = x_i$. In the limit where $\lambda \rightarrow \infty$, the sigmoid becomes a step function.

$$g(x) = A_g e^{\frac{-(x-\bar{x})^2}{2\sigma^2}} \quad (5.1)$$

$$s(x) = \frac{A_s}{1 + e^{-\lambda(x-x_i)}} \quad (5.2)$$

721 Finally, a possible representation of a skew distribution is given by formula 5.3
 722 and is the product of 5.1 and 5.2. Naturally, here $A_{sk} = A_g \times A_s$ and represents
 723 the theoretical maximum in the limit where the skew tends to a gaussian function.

$$sk(x) = g(x) \times s(x) = A_{sk} \frac{e^{\frac{-(x-\bar{x})^2}{2\sigma^2}}}{1 + e^{-\lambda(x-x_i)}} \quad (5.3)$$

724 5.2.3.3 Results

725 Influence of T_{scint} on the muon distribution

726 Influence of T_{RPC} on the muon distribution

727 Influence of the telescope inclination on the muon distribution

728 Comparison to data taken at GIF without irradiation

729 **5.2.4 Photon flux at GIF**

730 **5.2.4.1 Expectations from simulations**

731 In order to understand and evaluate the γ flux in the GIF area, simulations had been
 732 conducted in 1999 and published by S. Agosteo et al [6]. Table 5.1 presented in
 733 this article gives us the γ flux for different distances D to the source. This sim-
 734 ulation was done using GEANT and a Monte Carlo N-Particle (MCNP) transport
 735 code, and the flux F is given in number of γ per unit area and unit time along with
 736 the estimated error from these packages expressed in %.

Nominal ABS	Photon flux F [$s^{-1}cm^{-2}$]			
	at $D = 50$ cm	at $D = 155$ cm	at $D = 300$ cm	at $D = 400$ cm
1	$0.12 \cdot 10^8 \pm 0.2\%$	$0.14 \cdot 10^7 \pm 0.5\%$	$0.45 \cdot 10^6 \pm 0.5\%$	$0.28 \cdot 10^6 \pm 0.5\%$
2	$0.68 \cdot 10^7 \pm 0.3\%$	$0.80 \cdot 10^6 \pm 0.8\%$	$0.25 \cdot 10^6 \pm 0.8\%$	$0.16 \cdot 10^6 \pm 0.6\%$
5	$0.31 \cdot 10^7 \pm 0.4\%$	$0.36 \cdot 10^6 \pm 1.2\%$	$0.11 \cdot 10^6 \pm 1.2\%$	$0.70 \cdot 10^5 \pm 0.9\%$

Table 5.1: Total photon flux ($E\gamma \leq 662$ keV) with statistical error predicted considering a ^{137}Cs activity of 740 GBq at different values of the distance D to the source along the x-axis of irradiation field [6].

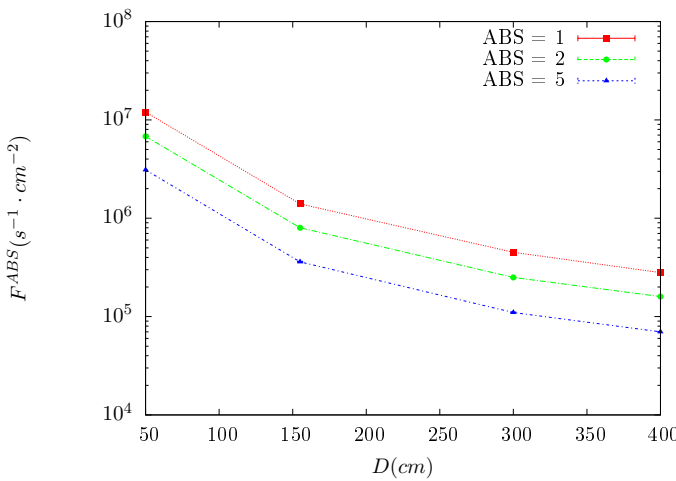


Figure 5.12: γ flux $F(D)$ is plot using values from table 5.1. As expected, the plot shows similar attenuation behaviours with increasing distance for each absorption factors.

737 The simulation doesn't directly provides us with an estimated flux at the level
 738 of our RPC. First of all, it is needed to extract the value of the flux from the
 739 available data contained in the original paper and then to estimate the flux in 2014
 740 at the time the experimentation took place. Figure 5.12 that contains the data from

741 Table 5.1. In the case of a pointlike source emitting isotropic and homogeneous
 742 gamma radiations, the gamma flux F at a distance D to the source with respect
 743 to a reference point situated at D_0 where a known flux F_0 is measured will be
 744 expressed like in Equation 5.4, assuming that the flux decreases as $1/D^2$, where c
 745 is a fitting factor.

$$F^{ABS} = F_0^{ABS} \times \left(\frac{cD_0}{D} \right)^2 \quad (5.4)$$

746 By rewriting Equation 5.4, it comes that :

$$c = \frac{D}{D_0} \sqrt{\frac{F^{ABS}}{F_0^{ABS}}} \quad (5.5)$$

$$\Delta c = \frac{c}{2} \left(\frac{\Delta F^{ABS}}{F^{ABS}} + \frac{\Delta F_0^{ABS}}{F_0^{ABS}} \right) \quad (5.6)$$

747 Finally, using Equation 5.5 and the data in Table 5.1 with $D_0 = 50$ cm as
 748 reference point, we can build Table 5.2. It is interesting to note that c for each
 749 value of D doesn't depend on the absorption factor.

Nominal ABS	Correction factor c		
	at $D = 155$ cm	at $D = 300$ cm	at $D = 400$ cm
1	$1.059 \pm 0.70\%$	$1.162 \pm 0.70\%$	$1.222 \pm 0.70\%$
2	$1.063 \pm 1.10\%$	$1.150 \pm 1.10\%$	$1.227 \pm 0.90\%$
5	$1.056 \pm 1.60\%$	$1.130 \pm 1.60\%$	$1.202 \pm 1.30\%$

Table 5.2: Correction factor c is computed thanks to formulae 5.5 taking as reference $D_0 = 50$ cm and the associated flux F_0^{ABS} for each absorption factor available in table 5.1.

750 For the range of D/D_0 values available, it is possible to use a simple linear
 751 fit to get the evolution of c . The linear fit will then use only 2 free parameters, a
 752 and b , as written in Equation 5.7. This gives us the results showed in Figure 5.13.
 753 Figure 5.13b confirms that using only a linear fit to extract c is enough as the
 754 evolution of the rate that can be obtained superimposes well on the simulation
 755 points.

$$c \left(\frac{D}{D_0} \right) = a \frac{D}{D_0} + b \quad (5.7)$$

$$F^{ABS} = F_0^{ABS} \left(a + \frac{bD_0}{D} \right)^2 \quad (5.8)$$

$$\Delta F^{ABS} = F^{ABS} \left[\frac{\Delta F_0^{ABS}}{F_0^{ABS}} + 2 \frac{\Delta a + \Delta b \frac{D_0}{D}}{a + \frac{bD_0}{D}} \right] \quad (5.9)$$

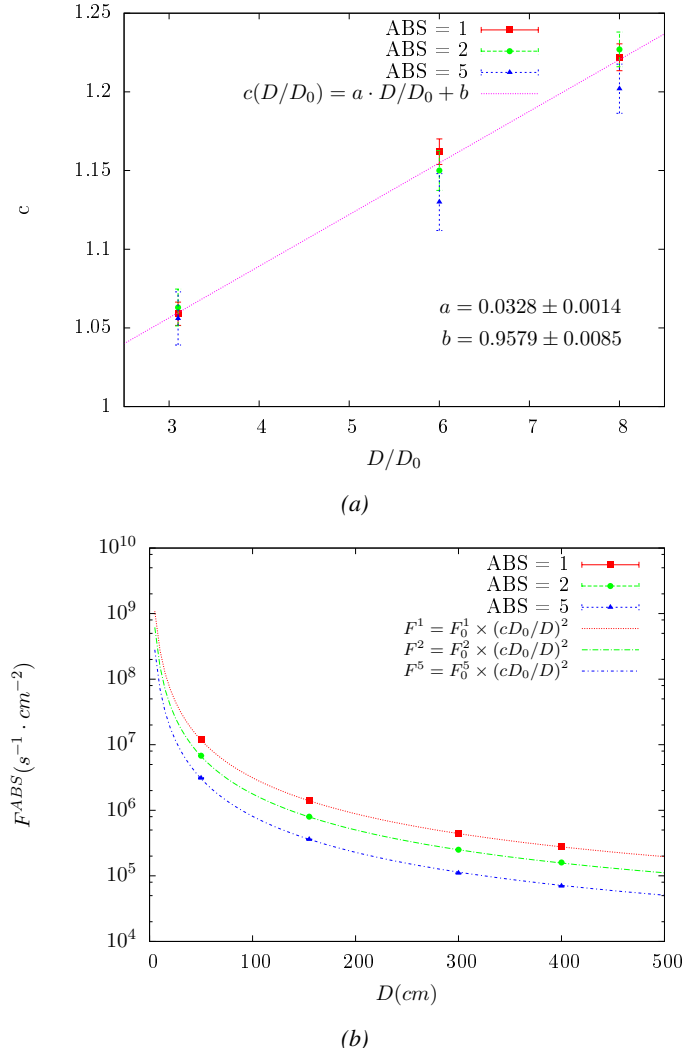


Figure 5.13: Figure 5.13a shows the linear approximation fit done via formulae 5.7 on data from table 5.2. Figure 5.13b shows a comparison of this model with the simulated flux using a and b given in figure 5.13a in formulae 5.4 and the reference value $D_0 = 50\text{cm}$ and the associated flux for each absorption factor F_0^{ABS} from table 5.1

In the case of the 2014 GIF tests, the RPC plane is located at a distance $D = 206$ cm to the source. Moreover, to estimate the strength of the flux in 2014, it is necessary to consider the nuclear decay through time associated to the Cesium source whose half-life is well known ($t_{1/2} = (30.05 \pm 0.08)$ y). The very first source activity measurement has been done on the 5th of March 1997 while the

761 GIF tests were done between the 20th and the 31st of August 2014, i.e. at a
 762 time $t = (17.47 \pm 0.02)$ y resulting in an attenuation of the activity from 740 GBq
 763 in 1997 to 494 GBq in 2014. All the needed information to extrapolate the flux
 764 through our detector in 2014 has now been assembled, leading to the Table 5.3. It
 765 is interesting to note that for a common RPC sensitivity to γ of $2 \cdot 10^{-3}$, the order
 766 of magnitude of the estimated hit rate per unit area is of the order of the kHz for
 767 the fully opened source. Moreover, taking profit of the two working absorbers, it
 768 will be possible to scan background rates at 0 Hz, ~ 300 Hz as well as ~ 600 Hz.
 769 Without source, a good estimate of the intrinsic performance will be available.
 770 Then at 300 Hz, the goal will be to show that the detectors fulfill the performance
 771 certification of CMS RPCs. Then a first idea of the performance of the detectors at
 772 higher background will be provided with absorption factors 2 (~ 600 Hz) and 1 (no
 773 absorption). *[Here I will also put a reference to the plot showing the estimated
 774 background rate at the level of RE3/I in the case of HL-LHC but this one being
 775 in another chapter, I will do it later.]*

Nominal ABS	Photon flux F [$s^{-1}cm^{-2}$]			Hit rate/unit area [$Hz cm^{-2}$] at $D^{2014} = 206$ cm
	at $D_0^{1997} = 50$ cm	at $D^{1997} = 206$ cm	at $D^{2014} = 206$ cm	
1	$0.12 \cdot 10^8 \pm 0.2\%$	$0.84 \cdot 10^6 \pm 0.3\%$	$0.56 \cdot 10^6 \pm 0.3\%$	1129 ± 32
2	$0.68 \cdot 10^7 \pm 0.3\%$	$0.48 \cdot 10^6 \pm 0.3\%$	$0.32 \cdot 10^6 \pm 0.3\%$	640 ± 19
5	$0.31 \cdot 10^7 \pm 0.4\%$	$0.22 \cdot 10^6 \pm 0.3\%$	$0.15 \cdot 10^6 \pm 0.3\%$	292 ± 9

Table 5.3: The data at D_0 in 1997 is taken from [6]. In a second step, using Equations 5.8 and 5.9, the flux at D can be estimated in 1997. Then, taking into account the attenuation of the source activity, the flux at D can be estimated at the time of the tests in GIF in 2014. Finally, assuming a sensitivity of the RPC to γ $s = 2 \cdot 10^{-3}$, an estimation of the hit rate per unit area is obtained.

776 **5.2.4.2 Dose measurements**

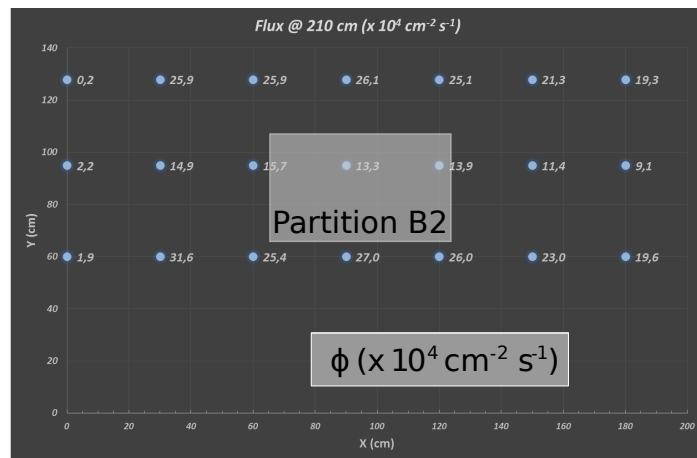


Figure 5.14: Dose measurements has been done in a plane corresponding to the tents front side. This plan is 1900 mm away from the source. As explained in the first chapter, a lens-shaped lead filter provides a uniform photon flux in the vertical plan orthogonal to the beam direction. If the second line of measured fluxes is not taken into account because of lower values due to experimental equipments in the way between the source and the tent, the uniformity of the flux is well showed by the results.

5.2.5 Results and discussions

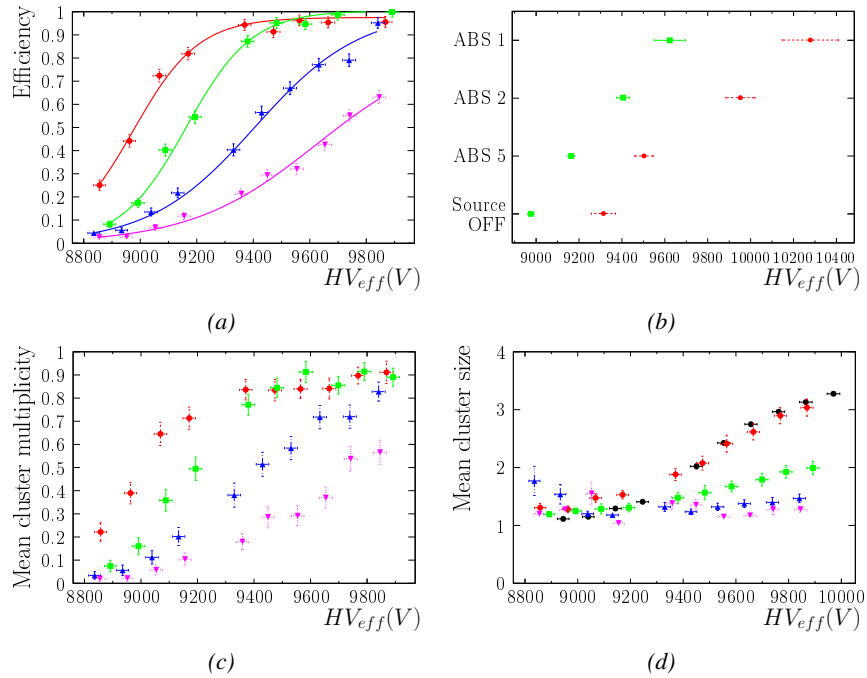


Figure 5.15

5.3 Longevity tests at GIF++

778 Longevity studies imply a monitoring of the performance of the detectors probed
779 using a high intensity muon beam in a irradiated environment by periodically mea-
780 suring their rate capability, the dark current running through them and the bulk
781 resistivity of the Bakelite composing their electrodes. GIF++, with its very intense
782 ^{137}Cs source, provides the perfect environment to perform such kind of tests. As-
783 suming a maximum acceleration factor of 3, it is expected to accumulate the equiv-
784 alent charge in 1.7 years.

785 As the maximum background is found in the endcap, the choice naturally was
786 made to focus the GIF++ longevity studies on endcap chambers. Most of the RPC
787 system was installed in 2007. Nevertheless, the large chambers in the fourth end-
788 cap (RE4/2 and RE4/3) have been installed during LS1 in 2014. The Bakelite of
789 these two different productions having different properties, four spare chambers
790 of the present system were selected, two RE2,3/2 spares and two RE4/2 spares.
791 Having two chambers of each type allows to always keep one of them non irradia-
792 ted as reference, the performance evolution of the irradiated chamber being then
793 compared through time to the performance of the non irradiated one.

794 The performance of the detectors under different level of irradiation is measured
795 periodically during dedicated test beam periods using the H4 muon beam. In be-
796 tween these test beam periods, the two RE2,3/2 and RE4/2 chambers selected for
797 this study are irradiated by the ^{137}Cs source in order to accumulate charge and
798 the gamma background is monitored, as well as the currents. The two remaining
799 chambers are kept non-irradiated as reference detectors. Due to the limited gas
800 flow in GIF++, the RE4 chamber remained non-irradiated until end of November
801 2016 where a new mass flow controller has been installed allowing for bigger vol-
802 umes of gas to flow in the system.

803 Figures 5.16 and 5.17 give us for different test beam periods, and thus for in-
804 creasing integrated charge through time, a comparison of the maximum efficiency,
805 obtained using a sigmoid-like function, and of the working point of both irradiated
806 and non irradiated chambers [8]. No aging is yet to see from this data, the shifts in
807 γ rate per unit area in between irradiated and non irradiated detectors and RE2 and
808 RE4 types being easily explained by a difference of sensitivity due to the various
809 Bakelite resistivities of the HPL electrodes used for the electrode production.

810 Collecting performance data at each test beam period allows us to extrapolate the
811 maximum efficiency for a background hit rate of 300 Hz/cm^2 corresponding to
812 the expected HL-LHC conditions. Aging effects could emerge from a loss of ef-
813 ficiency with increasing integrated charge over time, thus Figure 5.18 helps us
814 understand such degradation of the performance of irradiated detectors in compar-
815 ison with non irradiated ones. The final answer for an eventual loss of efficiency is
816 given in Figure 5.19 by comparing for both irradiated and non irradiated detectors

818 the efficiency sigmoids before and after the longevity study. Moreover, to complete
 819 the performance information, the Bakelite resistivity is regularly measured thanks
 820 to Ag scans (Figure 5.20) and the noise rate is monitored weekly during irradiation
 821 periods (Figure 5.21). At the end of 2016, no signs of aging were observed and
 822 further investigation is needed to get closer to the final integrated charge require-
 823 ments proposed for the longevity study of the present CMS RPC sub-system.

824

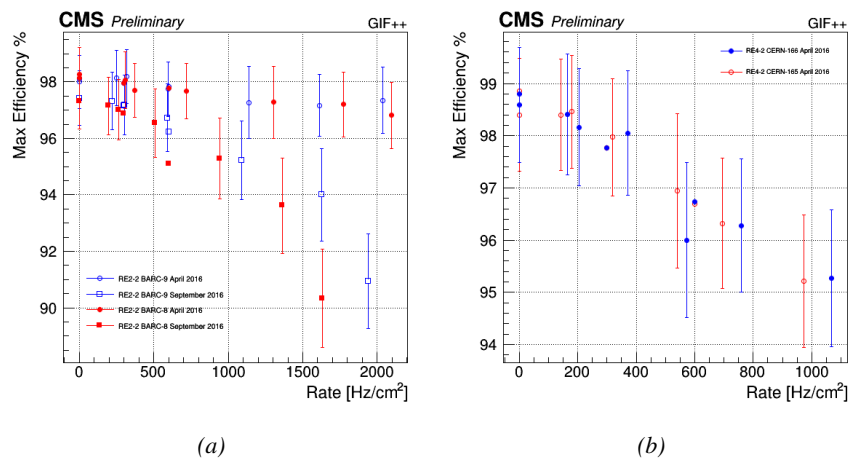


Figure 5.16: Evolution of the maximum efficiency for RE2 (5.16a) and RE4 (5.16b) chambers with increasing extrapolated γ rate per unit area at working point. Both irradiated (blue) and non irradiated (red) chambers are shown.

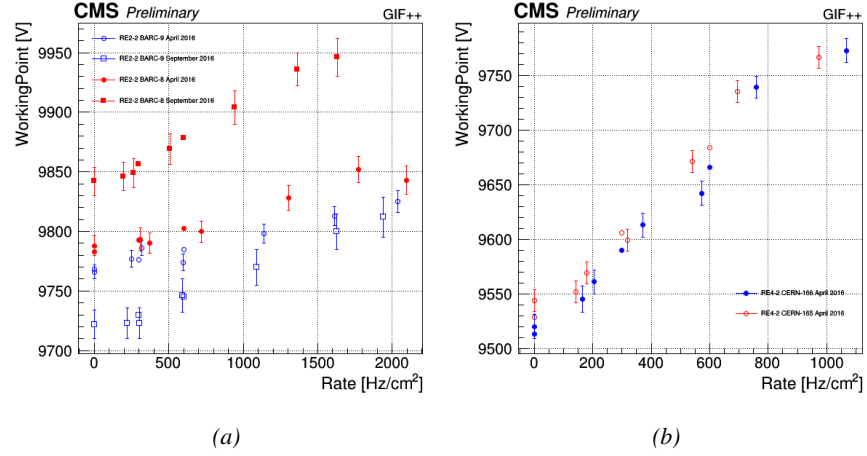


Figure 5.17: Evolution of the working point for RE2 (5.17a) and RE4 (5.17b) with increasing extrapolated γ rate per unit area at working point. Both irradiated (blue) and non irradiated (red) chambers are shown.

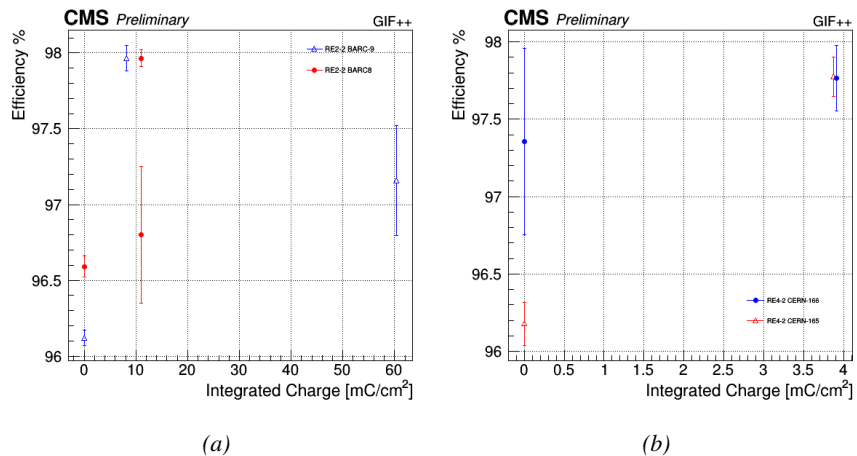


Figure 5.18: Evolution of the maximum efficiency at HL-LHC conditions, i.e. a background hit rate per unit area of 300 Hz/cm², with increasing integrated charge for RE2 (5.18a) and RE4 (5.18b) detectors. Both irradiated (blue) and non irradiated (red) chambers are shown. The integrated charge for non irradiated detectors is recorded during test beam periods and stays small with respect to the charge accumulated in irradiated chambers.

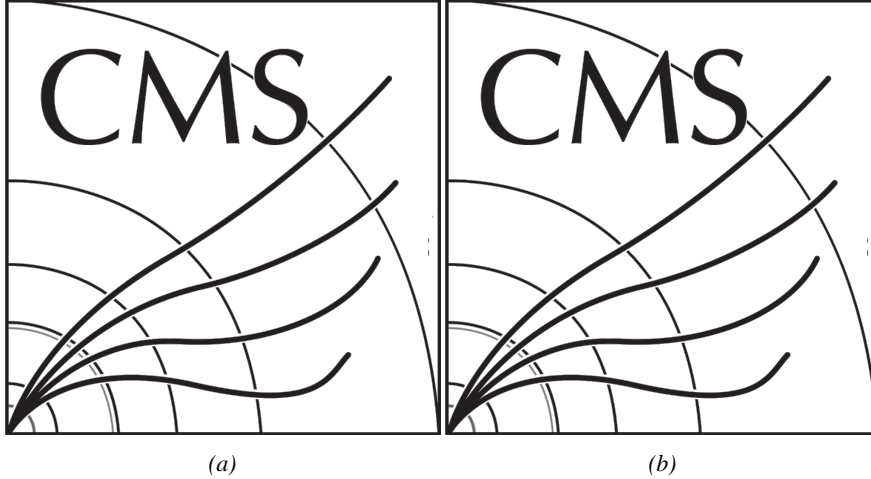


Figure 5.19: Comparison of the efficiency sigmoid before (triangles) and after (circles) irradiation for RE2 (5.19a) and RE4 (5.19b) detectors. Both irradiated (blue) and non irradiated (red) chambers are shown.

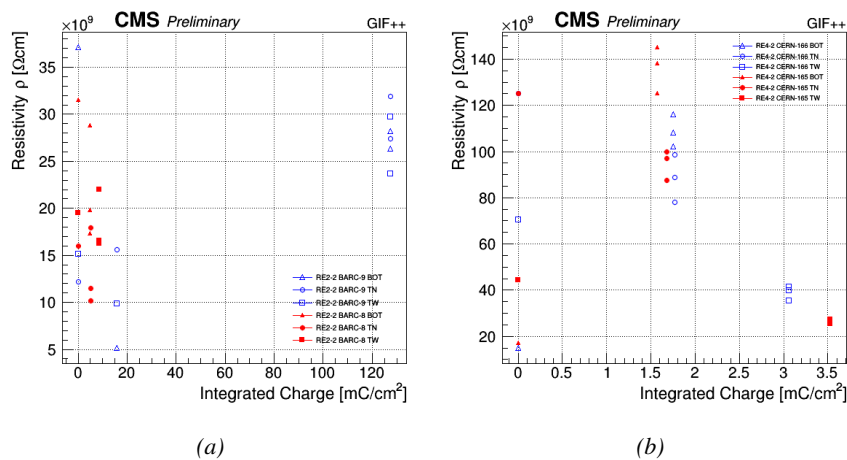


Figure 5.20: Evolution of the Bakelite resistivity for RE2 (5.20a) and RE4 (5.20b) detectors. Both irradiated (blue) and non irradiated (red) chambers are shown.

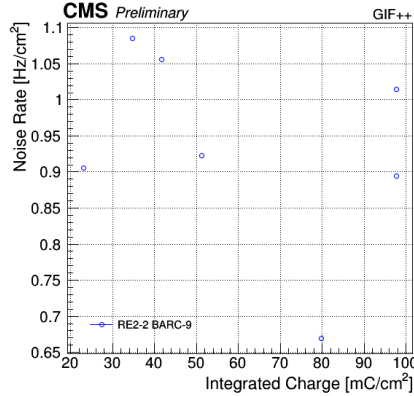


Figure 5.21: Evolution of the noise rate per unit area for the irradiated chamber RE2-2-BARC-9 only.

5.3.1 Description of the Data Acquisition

For the longevity studies, four spare chambers of the present system are used. Two spare RPCs of the RE2,3 stations as well as two spare RPCs from the new RE4 stations have been mounted in a Trolley. Six RE4 gaps are also placed in the trolley. The trolley is placed inside the GIF++ in the upstream region of the bunker, taking the cesium source as a reference. The trolley is oriented for the detection surface of the chambers to be orthogonal to the beam line. The system can be moved along the orthogonal plane in order to have the beam in all η -partitions. For the aging the trolley is moved outside the beam line and is placed in a distance of 5.2 m to the source, which irradiates the bunker using an attenuation filter of 2.2 which corresponds to a fluence of 10^7 gamma/cm².

During GIF++ operation, the data collected can be divided into different categories as several parameters are monitored in addition to the usual RPC performance data. On one hand, to know the performance of a chamber, it is need to measure its efficiency and to know the background conditions in which it is operated. To do this, the hit signals from the chamber are recorded and stored in a ROOT file via a Data Acquisition (DAQ) software. On the other hand, it is also very important to monitor parameters such as environmental pressure and temperature, gas temperature and humidity, RPC HV, LV, and currents, or even source and beam status. This is done through the GIF++ web Detector Control Software (DCS) that stores this information in a database.

Two different types of tests are conducted on RPCs via the DAQ. Indeed, the performance of the detectors is measured periodically during dedicated test beam periods using the H4 muon beam. In between these test beam periods, when the beam is not available, the chambers are irradiated by the ^{137}Cs in order to accu-

850 mulate deposited charge and the gamma background is measured.

851 RPCs under test are connected through LVDS cables to V1190A Time-to-
 852 Digital Converter (TDC) modules manufactured by CAEN. These modules, lo-
 853 cated in the rack area outside of the bunker, get the logic signals sent by the cham-
 854 bers and save them into their buffers. Due to the limited size of the buffers, the
 855 collected data is regularly erased and replaced. A trigger signal is needed for the
 856 TDC modules to send the useful data to the DAQ computer via a V1718 CAEN
 857 USB communication module.

858 In the case of performance test, the trigger signal used for data acquisition is
 859 generated by the coincidence of three scintillators. A first one is placed upstream
 860 outside of the bunker, a second one is placed downstream outside of the bunker,
 861 while a third one is placed in front of the trolley, close by the chambers. Every time
 862 a trigger is sent to the TDCs, i.e. every time a muon is detected, knowing the time
 863 delay in between the trigger and the RPC signals, signals located in the right time
 864 window are extracted from the buffers and saved for later analysis. Signals are
 865 taken in a time window of 400 ns centered on the muon peak (here we could show
 866 a time spectrum). On the other hand, in the case of background rate measurement,
 867 the trigger signal needs to be "random" not to measure muons but to look at gamma
 868 background. A trigger pulse is continuously generated at a rate of 300 Hz using a
 869 dual timer. To integrate an as great as possible time, all signals contained within
 870 a time window of 10us prior to the random trigger signal are extracted form the
 871 buffers and saved for further analysis (here another time spectrum to illustrate
 872 could be useful, maybe even place both spectrum together as a single Figure).

873 The signals sent to the TDCs correspond to hit collections in the RPCs. When a
 874 particle hits a RPC, it induce a signal in the pickup strips of the RPC readout. If this
 875 signal is higher than the detection threshold, a LVDS signal is sent to the TDCs.
 876 The data is then organised into 4 branches keeping track of the event number, the
 877 hit multiplicity for the whole setup, and the time and channel profile of the hits in
 878 the TDCs.

879 **5.3.2 RPC current, environmental and operation parameter mon-** 880 **itoring**

881 In order to take into account the variation of pressure and temperature between
 882 different data taking periods the applied voltage is corrected following the rela-
 883 tionship :

$$884 \quad HV_{eff} = HV_{app} \times \left(0.2 + 0.8 \cdot \frac{P_0}{P} \times \frac{T}{T_0} \right) \quad (5.10)$$

884 where T_0 (=293 K) and P_0 (=990 mbar) are the reference values.

885 5.3.3 Measurement procedure

- 886 Insert a short description of the online tools (DAQ, DCS, DQM).
- 887 Insert a short description of the offline tools : tracking and efficiency algorithm.
- 888 Identify long term aging effects we are monitoring the rates per strip.

889 5.3.4 Longevity studies results

6

890

891

Investigation on high rate RPCs

892 **6.1 Rate limitations and ageing of RPCs**

893 **6.1.1 Low resistivity electrodes**

894 **6.1.2 Low noise front-end electronics**

895 **6.2 Construction of prototypes**

896 **6.3 Results and discussions**

7

897

898

Conclusions and outlooks

899 **7.1 Conclusions**

900 **7.2 Outlooks**

References

901

- 902 [1] CERN. Geneva. LHC Experiments Committee. *The CMS muon project :
903 Technical Design Report*. Tech. rep. CERN-LHCC-97-032. CMS Collabora-
904 ration, 1997.
- 905 [2] CERN. Geneva. LHC Experiments Committee. *Technical Proposal for the
906 Phase-II Upgrade of the CMS Detector*. Tech. rep. CERN-LHCC-2015-010.
907 CMS Collaboration, 2015.
- 908 [3] CERN. Geneva. LHC Experiments Committee. *CMS, the Compact Muon
909 Solenoid : technical proposal*. Tech. rep. CERN-LHCC-94-38. CMS Col-
910 laboration, 1994.
- 911 [4] M. Abbrescia et al. “Study of long-term performance of CMS RPC under
912 irradiation at the CERN GIF”. In: *NIMA* 533 (2004), pp. 102–106.
- 913 [5] H.C. Kim et al. “Quantitative aging study with intense irradiation tests for
914 the CMS forward RPCs”. In: *NIMA* 602 (2009), pp. 771–774.
- 915 [6] S. Agosteo et al. “A facility for the test of large-area muon chambers at high
916 rates”. In: *NIMA* 452 (2000), pp. 94–104.
- 917 [7] PoS, ed. *CERN GIF ++ : A new irradiation facility to test large-area par-
918 ticle detectors for the high-luminosity LHC program*. Vol. TIPP2014. 2014,
919 pp. 102–109.
- 920 [8] M. Abbrescia et al. “Cosmic ray tests of double-gap resistive plate chambers
921 for the CMS experiment”. In: *NIMA* 550 (2005), pp. 116–126.
- 922 [9] A. Fagot. *GIF++ DAQ v4.0*. 2017. URL: https://github.com/afagot/GIF_DAQ.
- 924 [10] CAEN. *Mod. V1190-VX1190 A/B, 128/64 Ch Multihit TDC*. 14th ed. 2016.
- 925 [11] CAEN. *Mod. V1718 VME USB Bridge*. 9th ed. 2009.
- 926 [12] W-Ie-Ne-R. *VME 6021-23 VXI*. 5th ed. 2016.
- 927 [13] Wikipedia. *INI file*. 2017. URL: https://github.com/afagot/GIF_DAQ.
- 928

A

929

930 A data acquisition software for CAEN 931 VME TDCs

932 Certifying detectors in the perspective of HL-LHC required to develop tools for the
933 GIF++ experiment. Among them was the C++ Data Acquisition (DAQ) software
934 that allows to make the communications in between the computer and the TDC
935 modules in order to retrieve the RPC data [9]. In this appendix, details about the
936 software, as of how the software was written, how it functions and how it can be
937 exported to another similar setup.

938 **A.1 GIF++ DAQ file tree**

939 GIF++ DAQ source code is fully available on github at https://github.com/afagot/GIF_DAQ. The software requires 3 non-optional dependencies:

- 941 • CAEN USB Driver to mount the VME hardware
- 942 • CAEN VME Library to communicate with the VME hardware
- 943 • ROOT to organize the collected data into a TTree

944 The CAEN VME library will not be packaged by distributions and will need
945 to be installed manually. To compile the GIF++ DAQ project via a terminal, from
946 the DAQ folder use the command :

947 `make`

948 The source code tree is provided below along with comments to give an overview
 949 of the files' content. The different objects created for this project (v1718, v1190a,
 950 IniFile & DataReader) will be described in details in the following sections.

951



952 A.2 Description of the readout setup

953 The CMS RPC setup at GIF++ counts 5 V1190A Time-to-Digital Converter (TDC)
 954 manufactured by CAEN [10]. V1190A are VME units accepting 128 independent
 955 Multi-Hit/Multi-Event TDC channels whose signals are treated by 4 100 ps high
 956 performance TDC chips developped by CERN / ECP-MIC Division. The com-
 957 munication between the computer and the TDCs to transfer data is done via a
 958 V1718 VME master module also manufactured by CAEN and operated from a
 959 USB port [11]. These VME modules are all hosted into a 6U VME 6021 pow-

960 ered crate manufactured by W-Ie-Ne-R than can accomodate up to 21 VME bus
961 cards [12]. These 3 components of the DAQ setup are shown in Figure A.1.

962

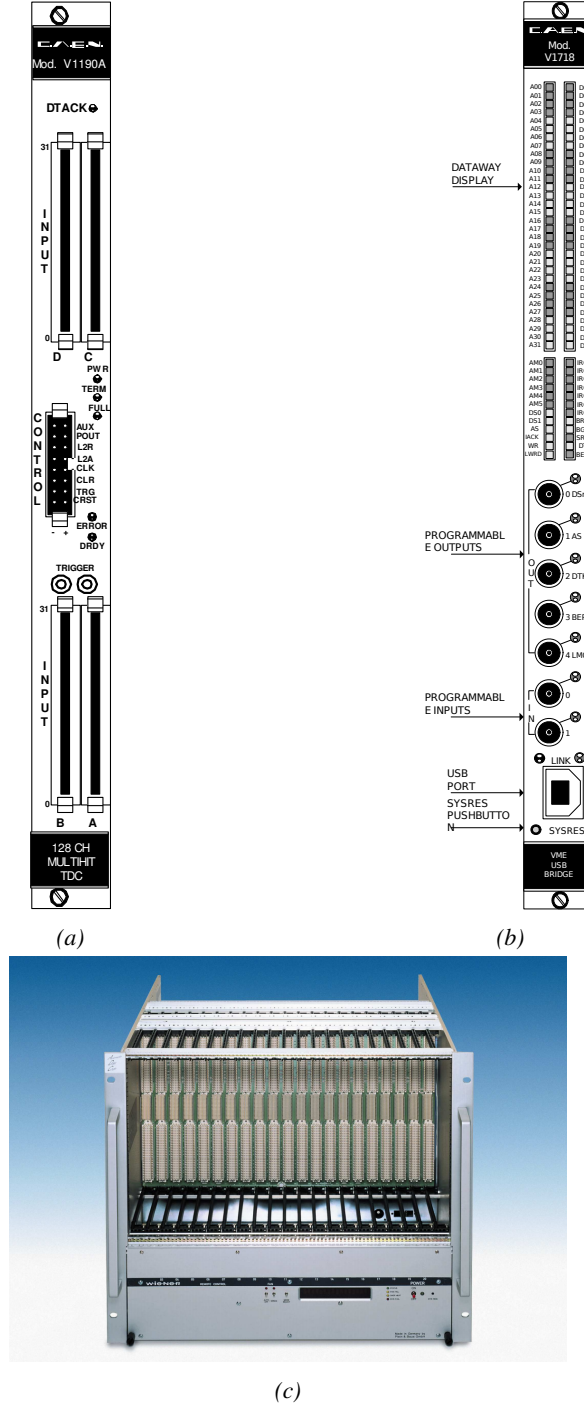


Figure A.1: (A.1a) View of the front panel of a V1190A TDC module [10]. (A.1b) View of the front panel of a V1718 Bridge module [11]. (A.1c) View of the front panel of a 6U 6021 VME crate [12].

963 A.3 Data read-out

964 To efficiently perform a data readout algorithm, C++ objects to handle the VME
 965 modules (TDCs and VME bridge) have been created along with objects to store
 966 data and read the configuration file that comes as an input of the DAQ software.
 967 It is useful to remind that the DAQ software in GIF++ is not a standalone software
 968 but is called through a Web Detector Control System (webDCS) application, that
 969 is the core of interactions with GIF++ setup, when data needs to be taken. Nev-
 970 ertheless, it is straight forward to make it into a standalone program that could be
 971 adapted to any VME setup using V1190A and V1718 modules.

972

973 A.3.1 V1190A TDCs

974 The DAQ used at GIF takes profit of the *Trigger Matching Mode* offered by V1190A
 975 modules. This setting is enabled through the method `v1190a::SetTrigMatching`
 976 (`int ntdcs`) where `ntdcs` is the total number of TDCs in the setup this setting
 977 needs to be enabled for (Source Code A.1). A trigger matching is performed in
 978 between a trigger time tag, a trigger signal sent into the TRIGGER input of the
 979 TDC visible on Figure A.1a, and the channel time measurements, signals recorded
 980 from the detectors under test in our case. Control over this data acquisition mode,
 981 explained through Figure A.2, is offered via 4 programmable parameters:

- 982 • **match window:** the matching between a trigger and a hit is done within a
 983 programmable time window. This is set via the method

984 `void v1190a::SetTrigWindowWidth(Uint windowHeight, int ntdcs)`

- 985 • **window offset:** temporal distance between the trigger tag and the start of
 986 the trigger matching window. This is set via the method

987 `void v1190a::SetTrigWindowWidth(Uint windowHeight, int ntdcs)`

- 988 • **extra search margin:** an extended time window is used to ensure that all
 989 matching hits are found. This is set via the method

990 `void v1190a::SetTrigSearchMargin(Uint searchMargin, int ntdcs)`

- 991 • **reject margin:** older hits are automatically rejected to prevent buffer over-
 992 flows and to speed up the search time. This is set via the method

993 `void v1190a::SetTrigRejectionMargin(Uint rejectMargin, int ntdcs)`

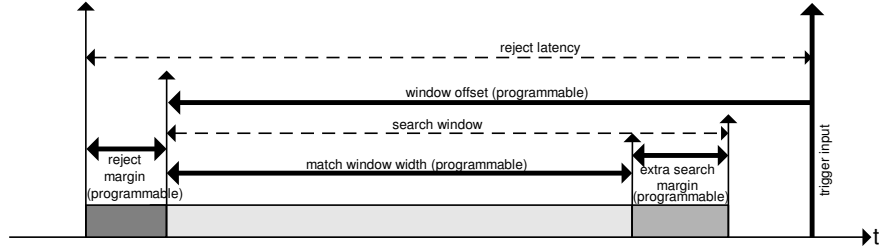


Figure A.2: Module V1190A Trigger Matching Mode timing diagram [10].

994 Each of these 4 parameters are given in number of clocks, 1 clock being 25 ns
 995 long. It is easy to understand at this level that there are 3 possible functioning
 996 settings:

- 997 • **1:** the match window is entirely contained after the trigger signal,
 998 • **2:** the match window overlaps the trigger signal, or
 999 • **3:** the match window is entirely contained before the trigger signal as dis-
 1000 played on Figure A.2.

1001 In both the first and second cases, the sum of the window width and of the
 1002 offset can be set to a maximum of 40 clocks, which corresponds to 1 μ s. Evidently,
 1003 the offset can be negative, allowing for a longer match window, with the constraint
 1004 of having the window ending at most 1 μ s after the trigger signal. In the third case,
 1005 the maximum negative offset allowed is of 2048 clocks (12 bit) corresponding to
 1006 51.2 μ s, the match window being strictly smaller than the offset. In the case of
 1007 GIF++, the choice has been made to use this last setting by delaying the trigger
 1008 signal. During the studies performed in GIF++, both the efficiency of the RPCs,
 1009 probed using a muon beam, and the noise or gamma background rate are moni-
 1010 tored. The extra search and reject margins are left unused.
 1011 To probe the efficiency of RPC detectors, the trigger time tag is provided by the
 1012 coïncidence of scintillators when a bunch of muons passes through GIF++ area is
 1013 used to trigger the data acquisition. For this measurement, it is useful to reduce the
 1014 match window width only to contain the muon information. Indeed, the delay in
 1015 between a trigger signal and the detection of the corresponding muon in the RPC
 1016 being very contant (typically a few tens of ns due to jitter and cable length), the
 1017 muon signals are very localised in time. Thus, due to a delay of approximalety
 1018 325 ns in between the muons and the trigger, the settings where chosen to have a
 1019 window width of 24 clocks (600 ns) centered on the muon peak thanks to a nega-
 1020 tive offset of 29 clocks (725 ns).
 1021 On the otherhand, monitoring the rates don't require for the DAQ to look at a
 1022 specific time window. It is important to integrate enough time to have a robust

1023 measurement of the rate as the number of hits per time unit. The triggerring signal
 1024 is provided by a pulse generator at a frequency of 300 Hz to ensure that the
 1025 data taking occurs in a random way, with respect to beam physics, to probe only
 1026 the irradiation spectrum on the detectors. The match window is set to 400 clocks
 1027 (10 µs) and the negative offset to 401 clocks as it needs to exceed the value of the
 1028 match window.

1029

Source Code A.1: Description of C++ object v1190a.

```

1030
1031 class v1190a
1032 {
1033     private :
1034         long             Handle;
1035         vector<Data32>   Address;
1036         CVDataWidth      DataWidth;
1037         CVAddressModifier AddressModifier;
1038
1039     public:
1040
1041         v1190a(long handle, IniFile *inifile, int ntdcs);
1042         ~v1190a();
1043         Data16 write_op_reg(Data32 address, int code, string error);
1044         Data16 read_op_reg(Data32 address, string error);
1045         void Reset(int ntdcs);
1046         void Clear(int ntdcs);
1047         void TestWR(Data16 value,int ntdcs);
1048         void CheckTDCStatus(int ntdcs);
1049         void CheckCommunication(int ntdcs);
1050         void SetTDCTestMode(Data16 mode,int ntdcs);
1051         void SetTrigMatching(int ntdcs);
1052         void SetTrigTimeSubtraction(Data16 mode,int ntdcs);
1053         void SetTrigWindowWidth(Uint windowHeight,int ntdcs);
1054         void SetTrigWindowOffset(Uint windowOffset,int ntdcs);
1055         void SetTrigSearchMargin(Uint searchMargin,int ntdcs);
1056         void SetTrigRejectionMargin(Uint rejectMargin,int ntdcs);
1057         void GetTrigConfiguration(int ntdcs);
1058         void SetTrigConfiguration(IniFile *inifile,int ntdcs);
1059         void SetTDCDetectionMode(Data16 mode,int ntdcs);
1060         void SetTDCResolution(Data16 lsb,int ntdcs);
1061         void SetTDCDeadTime(Data16 time,int ntdcs);
1062         void SetTDCHeadTrailer(Data16 mode,int ntdcs);
1063         void SetTDCEventSize(Data16 size,int ntdcs);
1064         void SwitchChannels(IniFile *inifile,int ntdcs);
1065         void SetIRQ(Data32 level, Data32 count,int ntdcs);
1066         void SetBlockTransferMode(Data16 mode,int ntdcs);
1067         void Set(IniFile *inifile,int ntdcs);
1068         void CheckStatus(CVErrorCodes status) const;
1069         int ReadBlockD32(Uint tdc, const Data16 address,
1070                          Data32 *data, const Uint words, bool ignore_berr);
1071         Uint  Read(RAWData *DataList,int ntdcs);
1072     };

```

1032 The v1190a object, defined in the DAQ software as in Source Code A.1, offers
 1033 the possibility to concatenate all TDCs in the readout setup into a single object con-

1034 taining a list of hardware addresses (addresses to access the TDCs' buffer through
 1035 the VME crate) and each constructor and method acts on the list of TDCs.

1036

1037 A.3.2 DataReader

1038 Enabled thanks to `v1190a::SetBlockTransferMode(Data16 mode, int ntdcs)`,
 1039 the data transfer is done via Block Transfer (BLT). Using BLT allows to tranfer a
 1040 fixed number of events called a *block*. This is used together with an Almost Full
 1041 Level (AFL) of the TDCs' output buffers, defined through `v1190a::SetIRQ(Data32`
 1042 `level, Data32 count, int ntdcs)`. This AFL gives the maximum amount of
 1043 32735 words (16 bits, corresponding to the depth of a TDC output buffer) that
 1044 can wrten in a buffer before an Interrupt Request (IRQ) is generated and seen by
 1045 the VME Bridge, stopping the data acquisition to transfer the content of each TDC
 1046 buffers before resuming. For each trigger, 6 words or more are written into the
 1047 TDC buffer:

1048 • a **global header** providing information of the event number since the begin-
 1049 ning of the data acquisition,

1050 • a **TDC header**,

1051 • the **TDC data** (*if any*), 1 for each hit recorded during the event, providing
 1052 the channel and the time stamp associated to the hit,

1053 • a **TDC error** providing error flags,

1054 • a **TDC trailer**,

1055 • a **global trigger time tag** that provides the absolute trigger time relatively
 1056 to the last reset, and

1057 • a **global trailer** providing the total word count in the event.

1058 As previously described in Section 4.4.3, CMS RPC FEEs provide us with
 1059 100 ns long LVDS output signals that are injected into the TDCs' input. Any
 1060 avalanche signal that gives a signal above the FEEs threshold is thus recorded by
 1061 the TDCs as a hit within the match window. Each hit is assigned to a specific TDC
 1062 channel with a time stamp, with a precision of 100 ps. The reference time, $t_0 = 0$,
 1063 is provided by the beginning of the match window. Thus for each trigger, coming
 1064 from a scintillator coïncidence or the pulse generator, a list of hits is stored into
 1065 the TDCs' buffers and will then be transferred into a ROOT Tree.

1066

1067 When the BLT is used, it is easy to understand that the maximum number of
 1068 words that have been set as ALF will not be a finite number of events or, at least,

1069 the number of events that would be recorded into the TDC buffers will not be a
 1070 multiple of the block size. In the last BLT cycle to tranfer data, the number of
 1071 events to transfer will most propably be lower than the block size. In that case, the
 1072 TDC can add fillers at the end of the block but this option requires to send more
 1073 data to the computer and is thus a little slower. Another solution is to finish the
 1074 transfer after the last event by sending a bus error that states that the BLT reached
 1075 the last event in the pile. This method has been chosen in GIF++.

1076
 1077 Due to irradiation, an event in GIF++ can count up to 300 words per TDC. A
 1078 limit of 4096 words (12 bits) has been set to generate IRQ which represent from
 1079 14 to almost 700 events depending on the average of hits collected per event. Then
 1080 the block size has been set to 100 events with enabled bus errors. When an AFL
 1081 is reached for one of the TDCs, the VME bridge stops the acquisition by sending
 1082 a BUSY signal.

1083
 1084 The data is then transferred one TDC at a time into a structure called `RAWData`
 1085 (Source Code A.2).

1086

1087 *Source Code A.2: Description of data holding C++ structure `RAWData`.*

```
1088 struct RAWData{
 1089   vector<int>           *EventList;
 1090   vector<int>           *NHitsList;
 1091   vector<int>           *QFlagList;
 1092   vector<vector<int>>    *ChannelList;
 1093   vector<vector<float>>  *TimeStampList;
 1094 };
```

1089 In order to organize the data transfer and the data storage, an object called
 1090 `DataReader` was created (Source Code A.3). On one hand, it has `v1718` and `v1190a`
 1091 objects as private members for communication purposes, such as VME modules
 1092 settings via the configuration file `*iniFile` or data read-out through `v1190a::Read()`
 1093 and on the other hand, it contains the struture `RAWData` that allows to organise the
 1094 data in vectors reproducing the tree structre of a ROOT file.

1095

1096 *Source Code A.3: Description of C++ object `DataReader`.*

```

class DataReader
{
    private:
        bool      StopFlag;
        IniFile *iniFile;
        Data32   MaxTriggers;
        v1718    *VME;
        int       nTDCs;
        v1190a   *TDCs;
        RAWData  TDCData;

    public:
        DataReader();
        virtual ~DataReader();
        void     SetIniFile(string inifilename);
        void     SetMaxTriggers();
        Data32  GetMaxTriggers();
        void     SetVME();
        void     SetTDC();
        int      GetQFlag(Uint it);
        void     Init(string inifilename);
        void     FlushBuffer();
        void     Update();
        string  GetFileName();
        void     WriteRunRegistry(string filename);
        void     Run();
};

1098     Each event is transferred from TDCData and saved into branches of a ROOT
1099    TTree as 3 integers that represent the event ID (EventCount), the number of hits
1100   read from the TDCs (nHits), and the quality flag that provides information for any
1101   problem in the data transfer (qflag), and 2 lists of nHits elements containing the
1102   fired TDC channels (TDCh) and their respective time stamps (TDCTS), as presented
1103   in Source Code A.4. An example of ROOT data file is provided with Figure A.3.
1104

```

Source Code A.4: Highlight of the data transfer and organisation within `DataReader::Run()` after the data has been collected into `TDCData`.

```
RAWData TDCData;
TFile *outputFile = new TFile(outputFileName.c_str(), "recreate");
TTree *RAWDataTree = new TTree("RAWData", "RAWData");

int EventCount = -9;
int nHits = -8;
int qflag = -7;
vector<int> TDCCh;
vector<float> TDCTS;

RAWDataTree->Branch("EventNumber", &EventCount, "EventNumber/I");
RAWDataTree->Branch("number_of_hits", &nHits, "number_of_hits/I");
RAWDataTree->Branch("Quality_flag", &qflag, "Quality_flag/I");
RAWDataTree->Branch("TDC_channel", &TDCCh);
RAWDataTree->Branch("TDC_TimeStamp", &TDCTS);

for(UInt i=0; i<TDCData.EventList->size(); i++) {
    EventCount = TDCData.EventList->at(i);
    nHits = TDCData.NHitsList->at(i);
    qflag = TDCData.QFlagList->at(i);
    TDCCh = TDCData.ChannelList->at(i);
    TDCTS = TDCData.TimeStampList->at(i);
    RAWDataTree->Fill();
}

//...
//Here read the TDC data using v1190a::Read() and place it into
//TDCData for as long as you didn't collect the requested amount
//of data.
//...
```

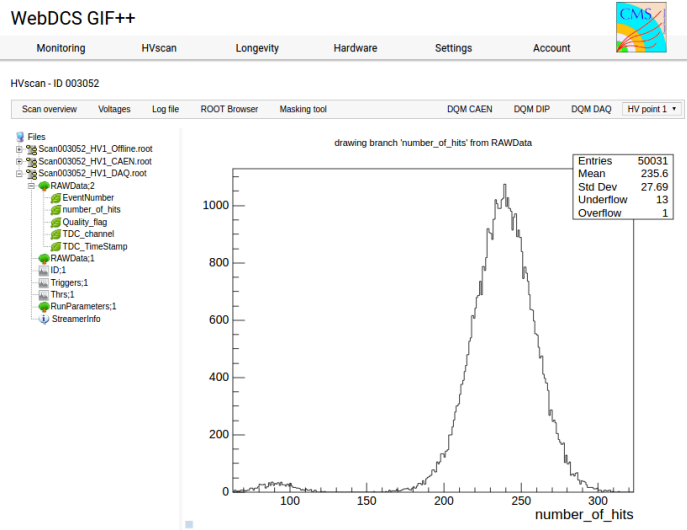


Figure A.3: Structure of the ROOT output file generated by the DAQ. The 5 branches (EventNumber, number_of_hits, Quality_flag, TDC_channel and TDC_TimeStamp) are visible on the left panel of the ROOT browser. On the right panel is visible the histogram corresponding to the variable nhits. In this specific example, there were approximately 50k events recorded to measure the gamma irradiation rate on the detectors. Each event is stored as a single entry in the TTree.

1107 A.4 Communications

1108 To ensure data readout and dialog in between the machine and the TDCs or in
 1109 between the webDCS and the DAQ, different communication solutions were used.
 1110 First of all, it is important to have a module to allow the communication in between
 1111 the TDCs and the computer from which the DAQ operates. When this communica-
 1112 tion is effective, shifters using the webDCS to control data taking can thus send
 1113 instructions to the DAQ.

1114

1115 A.4.1 V1718 USB Bridge

1116 In the previous section, the data transfer as been discussed. The importance of
 1117 the v1718 object (Source Code A.5), used as private member of DataReader,
 1118 was not explicited. VME master modules are used for communication purposes
 1119 as they host the USB port that connects the powered crate buffer to the com-
 1120 puter were the DAQ is installed. From the source code point of view, this ob-
 1121 ject is used to control the communication status, by reading the returned error
 1122 codes with v1718::CheckStatus(), or to check for IRQs coming from the TDCs

1123 through `v1718::CheckIRQ()`. Finally, to ensure that triggers are blocked at the
 1124 hardware level, a NIM pulse is sent out of one of the 5 programmable outputs
 1125 (`v1718::SendBUSY()`) to the VETO of the coincidence module where the trigger
 1126 signals originate from. As long as this signal is ON, no trigger can reach the TDCs
 1127 anymore.

1128

1129 *Source Code A.5: Description of C++ object v1718.*

```

class v1718{
    private:
        int Handle;
        Data32 Data;           // Data
        CVIRQLevels Level;     // Interrupt level
        CVAddressModifier AM;   // Addressing Mode
        CVDataWidth DataSize;   // Data Format
        Data32 BaseAddress;    // Base Address

    public:
        v1718(IniFile *inifile);
        ~v1718();
        long GetHandle(void) const;
        int SetData(Data16 data);
        Data16 GetData(void);
        int SetLevel(CVIRQLevels level);
        CVIRQLevels GetLevel(void);
        int SetAM(CVAddressModifier am);
        CVAddressModifier GetAM(void);
        int SetDatasize(CVDataWidth datasize);
        CVDataWidth GetDataSize(void);
        int SetBaseAddress(Data16 baseaddress);
        Data16 GetBaseAddress(void);
        void CheckStatus(CVErrorCodes status) const;
        void CheckIRQ();
        void SetPulsers();
        void SendBUSY(BusyLevel level);
};
```

1131 A.4.2 Configuration file

1132 The DAQ software takes as input a configuration file written using INI standard [13].
 1133 This file is partly filled with the information provided by the shifters when starting
 1134 data acquisition using the webDCS, as shown by Figure A.4. This information is
 1135 written in section `[General]` and will later be stored in the ROOT file that con-
 1136 tains the DAQ data as can be seen from Figure A.3. Indeed, another `TTree` called
 1137 `RunParameters` as well as the 2 histograms `ID`, containing the scan number, start
 1138 and stop time stamps, and `Triggers`, containing the number of triggers requested
 1139 by the shifter, are available in the data files.

Chamber	R32-2-NPD-BARC-#	R32-2-CERN-106	R32-2-NPD-BARC-3	R34-2-CERN-105	R34-2-XCOCBLL-14	Max triggers
HVcet 1	8600	8500	8600	8500	6500	
HVcet 2	8700	8600	8700	8600	6600	
HVcet 3	8800	8700	8800	8700	6700	
HVcet 4	8900	8800	8900	8800	6800	
HVcet 5	9000	8900	9000	8900	6900	
HVcet 6	9100	9000	9100	9000	7000	
HVcet 7	9200	9100	9200	9100	7100	
HVcet 8	9300	9200	9300	9200	7200	
HVcet 9	9400	9300	9400	9300	7300	
HVcet 10	9500	9400	9500	9400	7400	

Start HV scan

Figure A.4: WebDCS DAQ scan page. On this page, shifters need to choose the type of scan (Rate, Efficiency or Noise Reference scan), the gamma source configuration at the moment of data taking, the beam configuration, and the trigger mode. These information will be stored in the DAQ ROOT output. Are also given the minimal measurement time and waiting time after ramping up of the detectors is over before starting the data acquisition. Then, the list of HV points to scan and the number of triggers for each run of the scan are given in the table underneath.

1140 The rest of the information is written beforehand in the configuration file template,
 1141 as explicited in Source Code A.6, and contains the hardware addresses to
 1142 the different VME modules in the setup as well as settings for the TDCs. As the
 1143 TDC settings available in the configuration file are not supposed to be modified, an
 1144 improvement would be to remove them from the configuration file and to hardcode
 1145 them inside of the DAQ code itself or to place them into a different INI file that
 1146 would host only the TDC settings to lower the probability for a bad manipulation
 1147 of the configuration file that can be modified from one of webDCS' menus.
 1148

Source Code A.6: INI configuration file template for 4 TDCs. In section [**General1**], the number of TDCs is explicited and information about the ongoing run is given. Then, there are sections for each and every VME modules. There buffer addresses are given and for the TDCs, the list of channels to enable is given. Finally, in section [**TDCSettingsJ**], a part of the TDC settings are given.
 1149

```

[General]
Tdcஸ=4
ScanId=$scanid
HV=$HV
RunType=$runtype
MaxTriggers=$maxtriggers
Beam=$beam
[VMEInterface]
Type=V1718
BaseAddress=0XF0000
Name=VmeInterface
[TDC0]
Type=V1190A
BaseAddress=0x00000000
Name=Tdc0
StatusA00-15=1
StatusA16-31=1
StatusB00-15=1
StatusB16-31=1
StatusC00-15=1
StatusC16-31=1
StatusD00-15=1
StatusD16-31=1
[TDC1]
Type=V1190A
BaseAddress=0x11110000
Name=Tdc1
StatusA00-15=1
StatusA16-31=1
StatusB00-15=1
StatusB16-31=1
StatusC00-15=1
StatusC16-31=1
StatusD00-15=1
StatusD16-31=1
1150 [TDC2]
Type=V1190A
BaseAddress=0x22220000
Name=Tdc2
StatusA00-15=1
StatusA16-31=1
StatusB00-15=1
StatusB16-31=1
StatusC00-15=1
StatusC16-31=1
StatusD00-15=1
StatusD16-31=1
[TDC3]
Type=V1190A
BaseAddress=0x44440000
Name=Tdc3
StatusA00-15=1
StatusA16-31=1
StatusB00-15=1
StatusB16-31=1
StatusC00-15=1
StatusC16-31=1
StatusD00-15=1
StatusD16-31=1
[TDCSettings]
TriggerExtraSearchMargin=0
TriggerRejectMargin=0
TriggerTimeSubtraction=0b1
TdcDetectionMode=0b01
TdcResolution=0b10
TdcDeadTime=0b00
TdcHeadTrailer=0b1
TdcEventSize=0b1001
TdcTestMode=0b0
BLTMode=1

```

1151 A.4.3 WebDCS/DAQ intercommunication

1152 When shifters send instructions to the DAQ via the configuration file, it is the web-
 1153 DCS itself that gives the start command to the DAQ and then the 2 softwares use
 1154 inter-process communication through file to synchronise themselves. This com-
 1155 munication file is represented by the variable `const string __runstatuspath`.

1156
 1157 On one side, the webDCS sends commands or status that are readout by the

1158 DAQ:

- 1159 • INIT, status sent when launching a scan and read via function `CtrlRunStatus(...)`,
- 1160 • START, command to start data taking and read via function `CheckSTART()`,
- 1161 • STOP, command to stop data taking at the end of the scan and read via
1162 function `CheckSTOP()`, and
- 1163 • KILL, command to kill data taking sent by user and read via function `CheckKILL()`
- 1164 and on the other, the DAQ sends status that are controled by the webDCS:
- 1165 • DAQ_RDY, sent with `SendDAQReady()` to signify that the DAQ is ready to
1166 receive commands from the webDCS,
- 1167 • RUNNING, sent with `SendDAQRunning()` to signify that the DAQ is taking
1168 data,
- 1169 • DAQ_ERR, sent with `SendDAQError()` to signify that the DAQ didn't receive
1170 the expected command from the webDCS or that the launch command didn't
1171 have the right number of arguments,
- 1172 • RD_ERR, sent when the DAQ wasn't able to read the communication file,
1173 and
- 1174 • WR_ERR, sent when the DAQ wasn't able to write into the communication
1175 file.

1176 **A.5 DAQ algorithm overview**

1177 **A.6 Software export**

B

1178

1179 Details on the online analysis package

1180 **B.1 Introduction**

1181 insert text here

C

1182

1183

1184

Structure of the hybrid simulation software

1185 C.1 Introduction

1186 insert text here...

